THE JOURNAL OF PHYSICAL CHEMISTRY C
A JOURNAL OF THE AMERICAN CHEMICAL SOCIETY

pubs.acs.org/JPCC

Article

Hot-Hole-Induced Molecular Scissoring: A Case Study of Plasmon-Driven Decarboxylation of Aromatic Carboxylates

Qingfeng Zhang, Kexun Chen, and Hui Wang*

Cite This: *J. Phys. Chem. C* 2021, 125, 20958–20971

Read Online

ACCESS | Metrics & More | Article Recommendations | Supporting Information

ABSTRACT: Optically excited plasmonic nanostructures may function as molecular scissors with unique capabilities to cleave specific chemical bonds in molecular adsorbates through either plasmon-enhanced intramolecular electronic excitations or injection of photoexcited hot electrons into adsorbate orbitals. Here we chose plasmon-driven decarboxylation of aromatic carboxylates as a model reaction system to demonstrate that plasmonic hot holes, instead of electrons, could also be effectively harnessed to trigger regioselective bond cleavage in molecular adsorbates. We used surface-enhanced Raman scattering as an *in situ* spectroscopic tool to precisely monitor the decarboxylation reactions in real time and further correlate the reaction kinetics to local-field enhancements. The apparent rate constants were proportional to the fourth power of the local-field enhancements and exhibited a superlinear dependence on the excitation powers. Such a non-linear power dependence of reaction rates was a hallmark of hot-carrier-driven reactions involving multiphoton absorption rather than photothermally triggered processes, as inferred by the results of Raman thermometry. The decarboxylation reactions took place only at the surface sites with local-field intensities exceeding a certain threshold value, whereas the molecules experiencing weaker local fields below the threshold remained essentially unreactive. With the aid of density functional theory calculations, we were able to further relate the experimentally observed pH dependence of reaction kinetics to the frontier orbital energies of the hole-accepting adsorbates and the redox potentials of the electron-accepting protons, both of which could be modulated by adjusting the pH of the reaction medium.

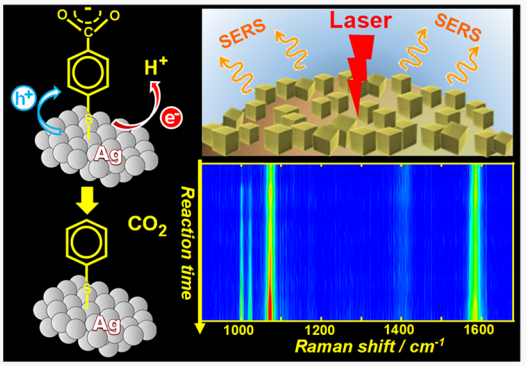

INTRODUCTION

The past decade has witnessed the emergence of plasmon-driven photocatalysis as a far-reaching paradigm shift in the fields of heterogeneous catalysis and surface photochemistry.[1−14] The optical excitation and decay of the collective free electron oscillations within the confinement of metallic nanostructures, also known as localized plasmon resonances, give rise to a unique set of intriguing nanoscale photophysical effects, such as amplification of optical cross sections, local-field enhancements, photothermal heating, and photoexcitation of far-from-equilibrium hot charge carriers.[2,4,6,15−18] These plasmon-derived effects can be judiciously harnessed to trigger photocatalytic transformations of molecular adsorbates through unique reaction channels inaccessible under thermal conditions.[1−14] Although the detailed mechanisms may vary drastically from reaction to reaction, plasmon-induced cleavage of specific chemical bonds represents a ubiquitous key step, in many cases the rate-limiting step, in a diverse range of plasmon-driven molecule-transforming processes.[19−29] The bond cleavage in a molecular adsorbate can be triggered by plasmons through two fundamentally distinct mechanisms, specifically plasmon-enhanced intramolecular electronic excitations[22,24−26,28] and interfacial transfer of plasmonic hot electrons.[19,21,27,29] Both mechanisms involve the photo-excitation of electrons into an anti-bonding orbital of the molecules adsorbed on the surfaces of metallic nanostructures,[3,6,7,19,21,22,24−28] through which the activation energy barriers for bond cleavage can be effectively reduced. The radiative plasmon decay leads to drastic enhancements of the scattering fields at the nanostructure surfaces, known as the plasmonic antenna effect. The intense scattering photons re-radiated from plasmonic nanoantennas can enhance intra-molecular electronic transitions when the electronic transitions in a molecular adsorbate are on resonance with the plasmons.[6,7,22,24−26,28] In contrast, the non-radiative decay of plasmon resonances opens up unique charge-carrier-mediated reaction channels involving either metal-to-adsorbate transfer of energetic hot electrons following Landau damping[2,10,19,21,27] or direct photoexcitation of hot electrons in strongly coupled

Received: August 13, 2021
Published: September 16, 2021

https://doi.org/10.1021/acs.jpcc.1c07177
J. Phys. Chem. C 2021, 125, 20958–20971

metal−adsorbate systems through chemical interface damping.[6,30,31]

It has recently been found that the plasmonic hot holes are also capable of inducing bond cleavage in molecular adsorbates, as exemplified by the plasmon-driven decarboxylation of 4-mercaptobenzoic acid (4-MBA) adsorbed on nanostructured metallic surfaces.[32] The discovery of this reaction can be traced back to the early 2000s when Michota and Bukowska[33] used surface-enhanced Raman scattering (SERS) to monitor the self-assembly of 4-MBA on Au and Ag electrode surfaces. In addition to the spectral features of 4-MBA, several characteristic SERS peaks of mono-substituted benzene derivatives were also clearly observed, indicating the production of thiophenol (TP) through decarboxylation of surface-adsorbed 4-MBA. Without fully recognizing the crucial roles of the plasmon resonances, they claimed that this decarboxylation reaction was chemically triggered by strong interactions of 4-MBA with the highly roughened metal surfaces. Zhao and co-workers,[34] however, provided an alternative interpretation, which involved the charge-transfer-induced chemical enhancement of SERS, with all of the newly emerged SERS peaks arguably assigned to the non-totally symmetric (b_2) modes of 4-MBA rather than the Raman signatures of TP. Although certain aspects of the experimental observations may be interpreted reasonably well in the context of the surface roughness and charge transfer effects, detailed kinetic studies revealed that the SERS spectral evolution essentially signified the photocatalytic decarboxylation of 4-MBA, a unique plasmon-driven molecular scissoring process.[35,36] By carefully analyzing the reaction kinetics at various excitation wavelengths in deliberately controlled reaction environments, Yoon and co-workers[32] proposed that this decarboxylation reaction was essentially induced by injection of hot holes into deprotonated 4-MBA (4-mercaptobenzoate anion). Compared to the hot-electron-driven reactions, the hot-hole-induced photocatalytic bond cleavage, however, remains a much less explored research area full of fundamentally intriguing open questions well worthy of detailed mechanistic studies.

This work aimed at unraveling how plasmon-derived photophysical effects dictate hot-hole-induced molecular scissoring processes through a detailed case study conducted on the plasmon-driven decarboxylation of aromatic carboxylates chemisorbed to nanostructured Ag surfaces. Use of SERS as an *in situ* spectroscopic tool[3,12,37,38] endowed us with unique capabilities not only to resolve the detailed structural evolution of the transforming molecules in real time but also to further correlate the reaction rates and yields with the local-field enhancements in the plasmonic hot spots. The time-resolved SERS results, further corroborated by density functional theory (DFT) calculations, shed light on several fundamentally important questions concerning the detailed underlying reaction mechanisms: (1) What is the relationship between the reaction rates and the local field enhancements? (2) What does the power dependence of the reaction rates imply? (3) What are the factors limiting the reaction yields achievable under specific reaction conditions? (4) How does the pH of the reaction medium influence the transfer of hot carriers? This work provides important insights that guide us to rationally optimize the efficacy of plasmonic hot carriers in catalyzing targeted interfacial molecular transformations.

METHODS

Assembly of SiO_2@Ag Suprananoparticles (SNPs). We assembled dual-functional SiO_2@Ag SNPs, which served as both the plasmonic photocatalysts and the SERS substrates. Carboxylate-functionalized SiO_2 beads with an average diameter of ∼1 μm were purchased from Bangs Laboratories. Monodisperse Ag nanocubes with an average edge length of 36 nm were synthesized following a protocol developed by Xia and co-workers.[39] The surfaces of the SiO_2 beads were densely decorated with Ag nanocubes to form SiO_2@Ag SNPs using a previously developed layer-by-layer assembly method.[40] The experimental details of the synthesis and structural characterizations of the SiO_2@Ag SNPs were presented in the Supporting Information.

Time-Resolved SERS Measurements. The SERS measurements were performed on individual 4-MBA- or 2-MBA-coated SiO_2@Ag SNPs, which were immobilized on poly-4-vinylpyridine-functionalized Si substrates as a sub-monolayer film of isolated particles[41,42] following a procedure described in greater detail in the Supporting Information. Time-resolved SERS spectra were collected using a Bayspec *Nomadic* Raman microscope built on an Olympus BX51 reflected optical system under 785 nm laser excitation in the confocal mode (focal spot size: 2 μm in diameter). A 50× dark field objective (NA = 0.5, WD = 10.6 mm, Olympus LMPLFLN-BD) was used for both Raman signal collection and dark-field scattering imaging. The Raman signals were collected in a back scattering configuration. The Raman band of the silicon wafer centered at 520.7 cm^{-1} was used as the standard reference for spectrometer calibration. The laser beam was focused on one SiO_2@Ag SNP each time for Raman spectral collection. The laser power was adjusted using neutral density filters. A power meter (Newport, model: PMKIT-05-01) was used to measure the power of the excitation laser focused on the samples. The spectral acquisition time was varied from 1 to 20 s under most experimental conditions. Typically, the plasmon-driven decarboxylation reactions occurred in an aqueous environment containing 1.0 mM K_2CO_3 (pH 10) at room temperature. The pHs of the reaction medium could be adjusted in the range 2−13 by mixing appropriate amounts of HCl and NaOH in the absence of K_2CO_3. The pH-controlled solutions were delivered into the reaction chambers using a flow cell with an inlet and an outlet similar to the ones we previously used for single-molecule fluorescence measurements[43] except that the reaction chambers were assembled on a silicon substrate instead of a polyethylene glycol-functionalized glass coverslip. The flow rate was kept at 0.1 mL min^{-1} during the time-resolved SERS measurements.

DFT Calculations. The Q-Chem software package (version 5.3.0) was used for the DFT calculations. The exchange-correlation functional B3LYP was used. The basis set of light atoms was 6-31+G**, while the effective core potential was employed with the basis set def2-svp for the heavy Ag atoms. The solvation model used was the polarizable continuum model (PCM). The medium surrounding the molecules was water, whose dielectric constant was set to be 78.39.

The Raman activities obtained from the raw data were converted to relative Raman intensities according to the equation below[44]

https://doi.org/10.1021/acs.jpcc.1c07177
J. Phys. Chem. C 2021, 125, 20958−20971

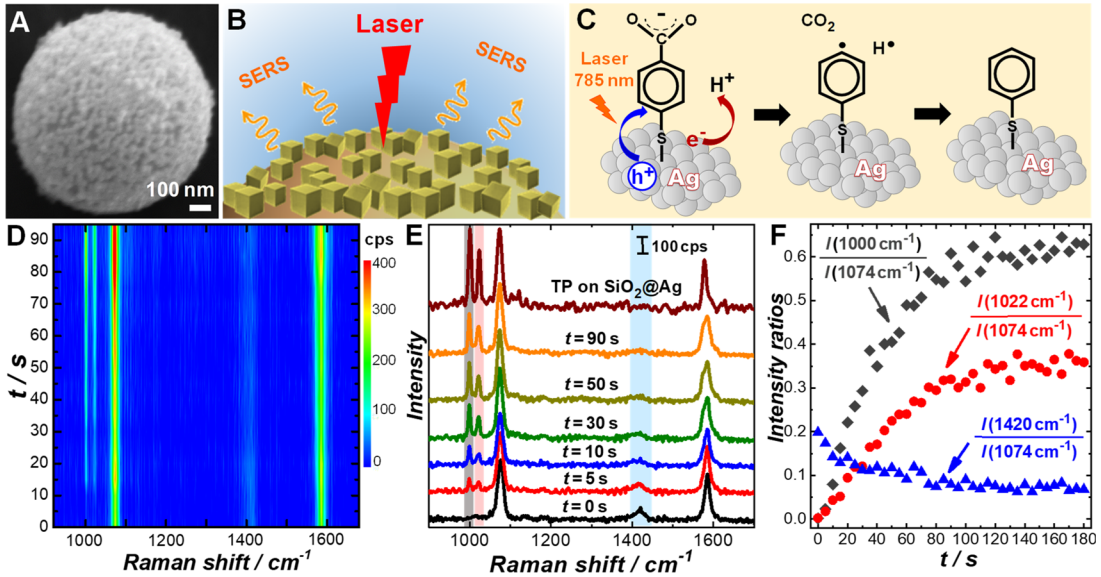

Figure 1. (A) SEM image of an individual SiO_2@Ag SNP. (B) Schematic illustration of using SERS to monitor the plasmon-driven reactions on SiO_2@Ag SNPs. (C) Schematic illustration of plasmon-driven decarboxylation of deprotonated 4-MBA chemisorbed on Ag surfaces. (D) Time-resolved SERS spectra collected on one 4-MBA-coated SiO_2@Ag SNP upon exposure to 785 nm laser illumination at a pH of 10 (in 1.0 mM K_2CO_3). The spectral acquisition time was 5 s, and the laser power was 1.1 mW. (E) Snapshot SERS spectra at reaction times of 0, 5, 10, 30, 50, and 90 s. The SERS spectrum of TP on a SiO_2@Ag SNP at a pH of 10 was also shown at the top for comparison. The spectra were offset for clarity, and the SERS intensities were expressed in units of counts per second (cps). (F) Temporal evolution of peak intensity ratios obtained from the time-resolved SERS results shown in panel D.

$$I_i = \frac{f(\nu_0 - \nu_i)^4 S_i}{\nu_i\left[1 - \exp\left(-\frac{hc\nu_i}{k_B T}\right)\right]} \quad (1)$$

where ν_0 was the frequency of the excitation laser, ν_i was the vibrational frequency of the ith normal mode, h was the Planck constant, c was the speed of light in a vacuum, k_B was the Boltzmann constant, and S_i was the Raman activity of the ith normal mode. f was an appropriately chosen common scaling factor for all peak intensities. In our calculations, the excitation frequency was set at 12738.85 cm^{-1}, which corresponded to the 785 nm excitation. A scaling factor of 1 was used for all of the peak intensities, and the temperature was set at 298.15 K.

The Raman intensity, I_i, was proportional to the absolute differential Raman scattering cross section, as shown in the following equation[45]

$$\left(\frac{d\sigma_i}{d\Omega}\right) = \frac{16\pi^4}{45}\frac{(\nu_0 - \nu_i)^4}{1 - \exp\left(-\frac{hc\nu_i}{k_B T}\right)}\frac{h}{8\pi^2 c\nu_i}S_i \quad (2)$$

where σ_i was the Raman scattering cross section of the ith vibrational mode and Ω represented the solid angle of light collection.

The Raman intensities were further expanded with the Lorentzian line shape shown below

$$L(x) = \frac{1}{\pi}\frac{\frac{1}{2}\Gamma}{(x - x_0)^2 + \left(\frac{1}{2}\Gamma\right)^2} \quad (3)$$

where x_0 was the center of the peak and Γ was a parameter specifying the peak width. Here we used a Γ value of 7 cm^{-1} as the full width at half-maximum (fwhm) of the Raman peaks.

RESULTS AND DISCUSSION

Under our experimental conditions, the plasmon-driven decarboxylation reactions occurred on the surfaces of SiO_2@Ag SNPs, which executed unique dual-functions as both plasmonic photocatalysts and SERS substrates under near-infrared excitations. The SiO_2@Ag SNPs (Figure 1A) were assembled by decorating the outer surfaces of dielectric SiO_2 beads (1.0 ± 0.014 μm in diameter, Figure S1 in the Supporting Information) with a layer of densely packed Ag nanocubes (36 ± 0.79 nm in edge length, Figure S2 in the Supporting Information) following a previously reported protocol.[40] Strong plasmon coupling among the densely packed Ag nanocubes[31,40] on SiO_2 bead surfaces gave rise to a broad plasmon resonance band in the optical extinction spectrum spanning the entire visible and much of the near-infrared regions (Figure S3 in the Supporting Information). Upon plasmonic excitations, interstitial hot spots with intense local field enhancements exploitable for both photocatalysis and SERS were created inside the nanoscale gaps between adjacent nanocubes.[15,31,40] The Ag surfaces were saturated with self-assembled monolayers of 4-MBA or 2-MBA by incubating the SiO_2@Ag SNPs with ethanoic solutions of the thiolated molecules. The SiO_2@Ag SNPs coated with 4-MBA or 2-MBA could be well-dispersed on a poly-4-vinylpyridine-functionalized Si substrate with interparticle distances typically beyond a few micrometers (Figure S4 in the Supporting Information). We focused a continuous-wave (CW) laser with an excitation wavelength (λ_{ex}) at 785 nm onto individual 4-MBA- or 2-MBA-coated SiO_2@Ag SNPs using a confocal Raman microscope (diameter of focal spot: ~2 μm), such that the molecule-transforming events could be monitored on one SNP at a time through time-resolved SERS measurements (see the schematic illustration in Figure 1B). The pH of the reaction medium was controlled by delivering aqueous solutions of 1.0 mM K_2CO_3 (pH 10) or HCl–NaOH mixtures

https://doi.org/10.1021/acs.jpcc.1c07177
J. Phys. Chem. C 2021, 125, 20958−20971

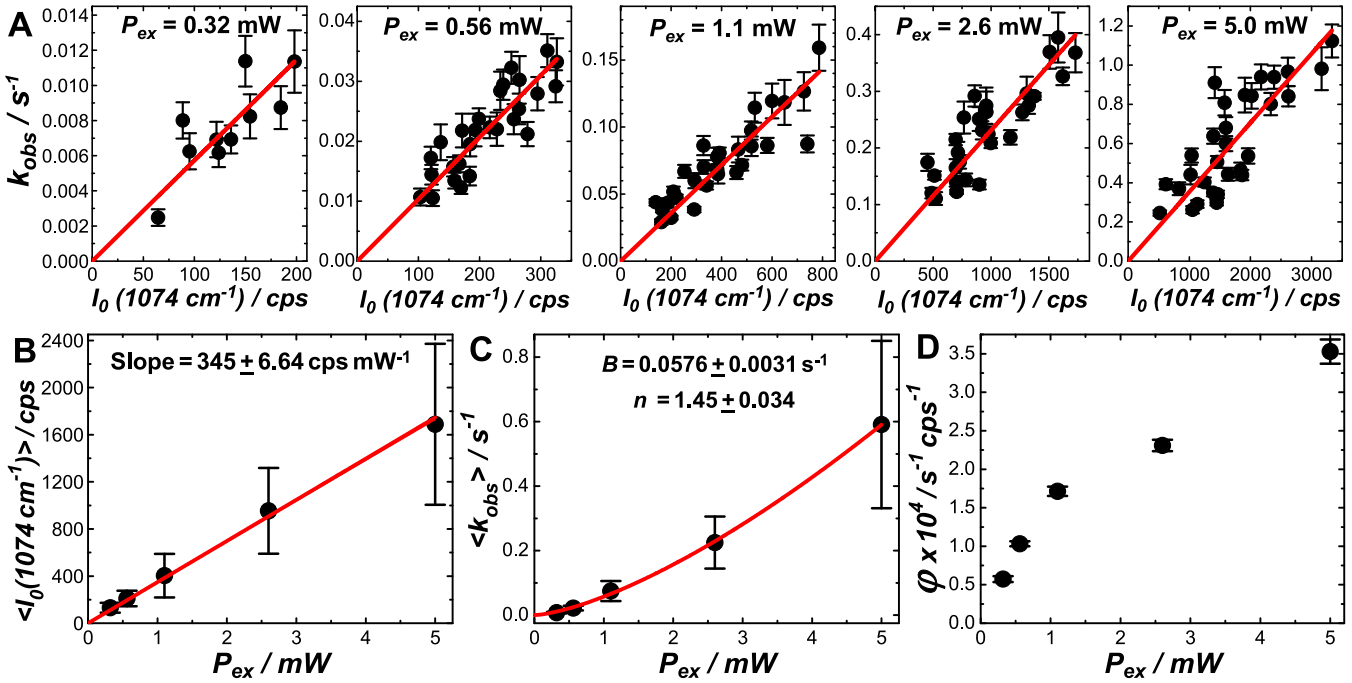

Figure 2. (A) Plots of k_{obs} vs the initial peak intensity of the ν(CS) mode, I_0(1074 cm^{-1}). The kinetic measurements were conducted at a fixed λ_{ex} value of 785 nm and five different P_{ex} values of 0.32, 0.56, 1.1, 2.6, and 5.0 mW. At each P_{ex}, the time-resolved SERS measurements were collected on different individual SiO_2@Ag SNPs one particle at a time. The error bars in panel A represent the standard deviations of the least-squares curve-fitting of each θ_{TP} trajectory. The k_{obs} values exhibited a linear relationship to I_0(1074 cm^{-1}), and the fitting results were shown as solid red lines in panel A. (B) Power dependence of ensemble-averaged I_0(1074 cm^{-1}). (C) Power dependence of ensemble-averaged k_{obs}. (D) Power dependence of the slope, φ, in panel A. The error bars in panel D represent the standard deviations of the least-squares curve-fitting results shown in panel A.

(adjustable pH ranging from 2 to 13) into a reaction chamber assembled on a SNPs/Si substrate.

Figure 1C schematically illustrates the hot carrier transfer processes and several transient intermediates involved in the plasmon-driven decarboxylation of 4-mercaptobenzoate. Optical excitation of the Ag plasmons at λ_{ex} of 785 nm led to the generation of hot electrons non-thermally distributed above the Fermi level of Ag, while leaving the energetic hot holes below the Fermi level. 4-Mercaptobenzoate chemisorbed on the Ag surfaces served as the hot hole acceptor, while the hot electrons were transferred to solution-phase protons to produce hydrogen atoms. The hot hole injection into 4-mercaptobenzoate led to the formation of a carboxyl radical intermediate, which underwent C−C bond cleavage to yield CO_2 and a thiophenyl radical. The surface-adsorbed thiophenyl radical was then rapidly combined with a hydrogen atom to form the final product, TP. 4-Mercaptobenzoate and TP displayed distinct spectral signatures clearly distinguishable in the SERS spectra, which enabled us to track the reaction progress through *in situ* SERS measurements. The well-defined peaks corresponding to the S−H stretching modes (centered at 2566 cm^{-1} for 4-MBA and at 2569 cm^{-1} for TP) in the normal Raman spectra became completely unobservable in the SERS spectra (Figure S5 in the Supporting Information), indicating that both the reactant and product molecules stayed chemisorbed to the Ag surfaces through covalent Ag−S interactions. Figure 1D shows the time-resolved SERS spectra collected from an individual 4-MBA-coated SiO_2@Ag SNP exposed to 1.0 mM K_2CO_3 aqueous solution (pH 10) under continuous laser illumination (785 nm, 1.1 mW). Several snapshot SERS spectra captured at various reaction times are shown in Figure 1E, and the temporal evolutions of the relative intensities of several characteristic SERS modes are plotted in Figure 1F. The Raman modes of 1000 and 1022 cm^{-1} were the spectral signatures of the mono-substituted benzene ring of TP,[32,36,46,47] both of which progressively increased in intensity as TP was produced. The SERS peak at 1420 cm^{-1} was assigned to the vibrational mode of COO^-, $\nu(COO^-)$,[48−50] whose intensity decreased over time during the reactions. The benzene ring mode, $\nu(CC_{ring})$, down-shifted from 1588 to 1578 cm^{-1} upon decarboxylation.[32,36] However, due to the limited spectral shift and the overlap of the two peaks, the $\nu(CC_{ring})$ mode was far from ideal for the quantification of the reactant and product fractions. The characteristic peak of the C−S stretching mode, ν(CS), was centered at 1074 cm^{-1} for both 4-MBA and TP,[32,36] and no spectral shift of the ν(CS) mode was observed during the reactions. The intensity of the ν(CS) mode gradually increased during the decarboxylation reactions (Figure 1D and Figure S6 in the Supporting Information), and there were several possible reasons for this: (1) The SERS signals of the ν(CS) mode of TP were intrinsically stronger than those of the 4-mercaptobenzoate. (2) There might be some orientational changes of the molecules induced by the decarboxylation reactions, causing changes in SERS intensities. (3) The interfacial reactions might cause changes of the local electron densities on the Ag surfaces, modifying the local plasmonic field enhancement to a certain extent. While the peak at 1000 cm^{-1} was absent for 4-mercaptobenzoate, it became almost equally intense as the ν(CS) peak at 1074 cm^{-1}, i.e., I(1000 cm^{-1}) ≈ I(1074 cm^{-1}), when all 4-mercaptobenzoate molecules were fully converted to TP (see Figures 1E and S5B in the Supporting Information). Therefore, the apparent fraction of the product, θ_{TP}, could be tracked as a function of reaction time, t, based on

https://doi.org/10.1021/acs.jpcc.1c07177
J. Phys. Chem. C 2021, 125, 20958−20971

the temporal evolution of the intensity ratio between the 1000 and 1074 cm^{-1} peaks, $I(1000\ cm^{-1})/I(1074\ cm^{-1})$. To investigate the power dependence of the reaction kinetics, the power of the excitation laser focused on the samples, P_{ex}, was tuned in the range from 320 μW to 5.0 mW. At each P_{ex}, the SERS-based kinetic measurements were repeated on multiple SiO_2@Ag SNPs *one particle at a time*. Instead of probing the transforming behaviors of a single molecule or a few molecules in a single hot spot, our time-resolved SERS results provided the ensemble-averaged kinetic information encompassing all molecular adsorbates in the plasmonic hot spots on each SNP. The θ_{TP} trajectories collected from individual SNPs might deviate significantly from each other even under exactly the same set of reaction conditions (Figure S7A−E in the Supporting Information) due to the intrinsic structural heterogeneity among the SNPs and the resulting particle-to-particle deviation of the averaged field enhancements. Although this reaction involved multiple elementary steps, the θ_{TP} trajectories collected from different particles at various P_{ex} values could all be well-described by a simple first-order kinetic model, strongly suggesting that the overall reaction kinetics were determined by a rate-limiting step. Considering the facts that the hydrogen atoms and thiophenyl radicals were both short-lived and the ultrafast hot carrier transfers took place typically on fs−ps time scales,[2,6,10,51,52] the rate-limiting step was most likely associated with the C−C bond cleavage. While the spectral evolution signifying the reactant-to-product conversion was well-resolved, none of the radical intermediates illustrated in Figure 1C were spectroscopically resolvable by SERS due to the short lifetimes of these transient species.

When comparing the ensemble-averaged trajectories of θ_{TP}, $\langle\theta_{TP}\rangle$, at various P_{ex} values (Figure S7F in the Supporting Information), we observed a general trend that both the reaction rate and yield increased with the P_{ex}. The observed first-order rate constant, k_{obs}, and the maximal reaction yield achievable at an infinitely long reaction time, $\theta_{t=\infty}$, were obtained by fitting the experimentally measured θ_{TP} trajectories with the following rate equation:

$$\theta_{TP}(t) = \theta_{t=\infty} \times (1 - e^{-k_{obs} \times t}) \quad (4)$$

Careful analysis of the time-resolved SERS results enabled us to correlate the k_{obs} and $\theta_{t=\infty}$ to the average field enhancements at the single SNP level. In Figure 2A, we plotted the values of k_{obs} obtained from individual 4-MBA-coated SiO_2@Ag SNPs as a function of the initial SERS intensities of the ν(CS) mode at 1074 cm^{-1}, $I_0(1074\ cm^{-1})$. We consistently observed that k_{obs} was linearly proportional to $I_0(1074\ cm^{-1})$ across the entire P_{ex} range under current investigations. None of the square, square root, or fourth root of $I_0(1074\ cm^{-1})$, however, held such linear proportionality to the k_{obs} (Figure S8 in the Supporting Information). In Raman scattering, the excitation laser impinging on the sample introduces an external electric field, $E_0(\omega_L)$, oscillating at the laser frequency of ω_L, which induces a dipole moment in the molecule oscillating at the Raman frequency of ω_R. The enhanced Raman intensity of a molecule, $I_{SERS}(\omega_L, \omega_R)$, is related to the Raman polarizability of the molecule, $\alpha(\omega_R, \omega_L)$, the signal-amplifying factor associated with the local field enhancement in the hot spot, G^{EM}, and the power of the excitation laser, $P_{ex}(\omega_L)$, as described by the following equation[53,54]

$$I_{SERS}(\omega_L, \omega_R) = C|\alpha(\omega_L, \omega_R)|^2 G^{EM} P_{ex}(\omega_L) \quad (5)$$

where C is a coefficient related to the signal collection efficiency of the optical system used for SERS measurements. The SERS signals can be enhanced either by increasing the amplitude of $\alpha(\omega_R, \omega_L)$ through chemical enhancement or by increasing the local electric field enhancement. G^{EM} is related to the local-field enhancements at both the excitation laser and the Raman scattering frequencies, as defined by the following equation[53,54]

$$G^{EM} = \left|\frac{E_{Loc}(\omega_L)}{E_0(\omega_L)}\right|^2 \left|\frac{E_{Loc}(\omega_R)}{E_0(\omega_R)}\right|^2 \quad (6)$$

where $E_{Loc}(\omega_L)$ and $E_{Loc}(\omega_R)$ represent the local field intensities at ω_L and ω_R, respectively. Due to the broad bandwidth of their plasmon resonances, the SiO_2@Ag SNPs displayed comparable field enhancements over a broad spectral range covering both the excitation and Raman emission wavelengths.[29,31] In this case, the SERS intensity of a molecule became approximately proportional to the fourth power of the local-field enhancement at the excitation wavelength

$$I_{SERS}(\omega_L, \omega_R) \propto \left|\frac{E_{Loc}(\omega_L)}{E_0(\omega_L)}\right|^4 \quad (7)$$

The SERS intensities of an ensemble of molecules depended not only on the local field enhancements but also on the numbers and orientations of the molecules being probed. For simplicity, we assumed that the total numbers of molecules and the averaged distributions of molecular orientations in the hot spots were about the same among different SiO_2@Ag SNPs. With such an assumption, the measured $I_0(1074\ cm^{-1})$ under our experimental conditions became approximately proportional to the fourth power of the average local-field enhancement, $|E_{Loc}(\omega_L)/E_0(\omega_L)|^4$, on each SiO_2@Ag SNP. The results shown in Figure 2A clearly revealed a linear proportionality of k_{obs} to the average $|E_{Loc}(\omega_L)/E_0(\omega_L)|^4$ at the single SNP level. The slope, φ, of the linear curve fitting results in each panel of Figure 2A reflected how sensitive k_{obs} was to the variation of the average $|E_{Loc}(\omega_L)/E_0(\omega_L)|^4$ on individual SiO_2@Ag SNPs at each P_{ex}. It is worth mentioning that the relationships between reaction rates and local-field enhancements are intimately tied to the detailed reaction mechanisms and, thus, may vary drastically from reaction to reaction. Even for the same plasmon-driven reaction, highly divergent results may be observed upon subtle variation of the photocatalyst structures and detailed reaction conditions, as manifested by the *para*-nitrothiophenol coupling reactions driven by plasmonic hot electrons.[55−58] Although a simple linear relationship between k_{obs} and $|E_{Loc}(\omega_L)/E_0(\omega_L)|^4$ was clearly observed for this plasmon-driven decarboxylation reaction, it may not be readily applicable to other plasmon-mediated molecular transformations. For many plasmon-driven photocatalytic reactions, it is challenging to completely distinguish the effects of hot carriers vs local field enhancements because the abundance of hot carriers is tied to the local field enhancements. In some other cases, the photocatalytic reactions can be purely driven by the enhanced near-fields on the nanostructure surfaces without the involvement of hot carriers.[59,60] The dependency of the reaction rates on the local field enhancements is a critical factor we should carefully consider when designing metallic nanophotocatalysts for specific plasmon-driven reactions, and the time-resolved SERS provides a generic spectroscopic tool enabling us to

https://doi.org/10.1021/acs.jpcc.1c07177
J. Phys. Chem. C 2021, 125, 20958−20971

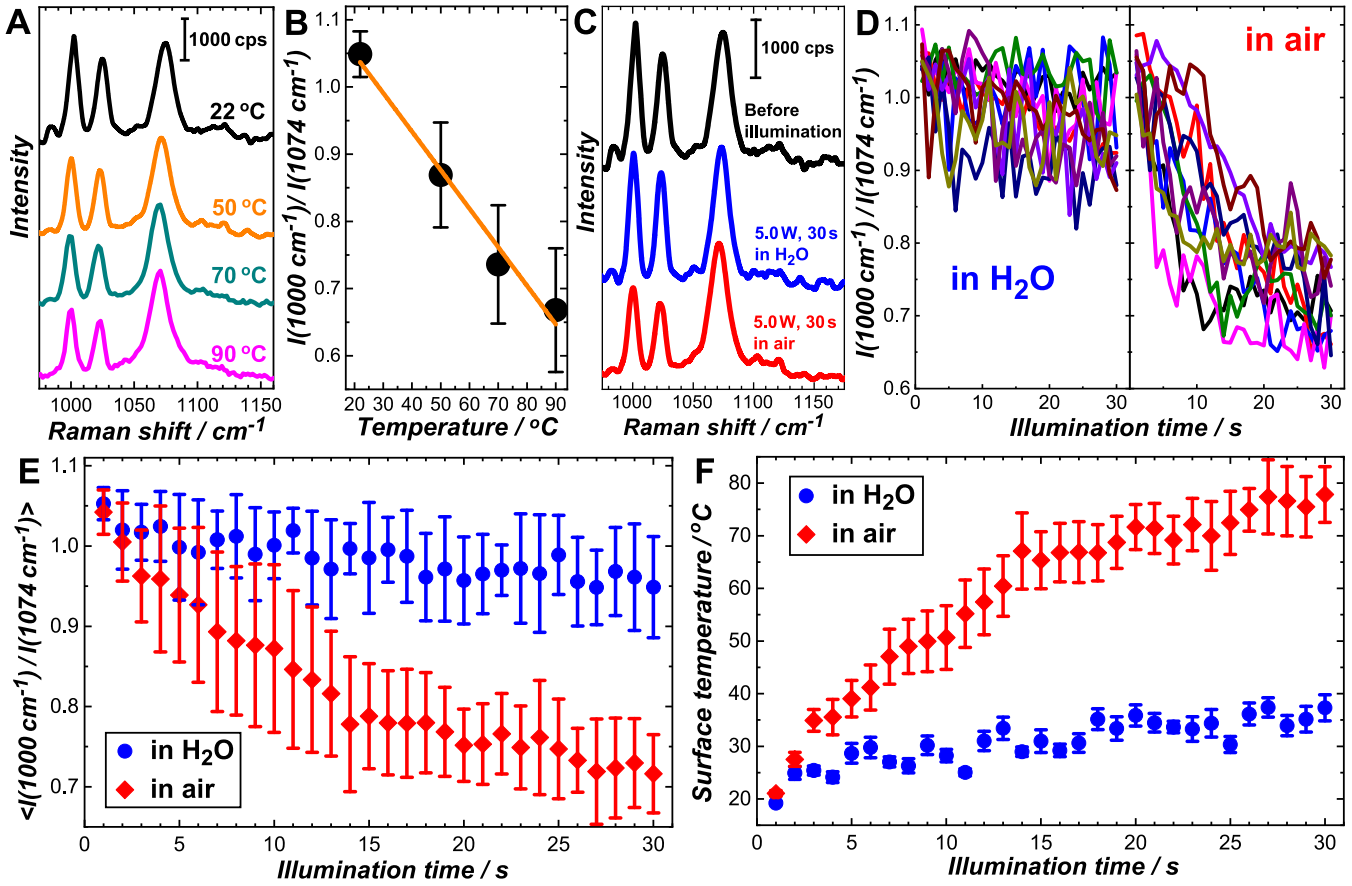

Figure 3. (A) Representative SERS spectra of TP on individual SiO_2@Ag SNPs after being thermally heated at different temperatures for 30 min. The SERS spectra were collected at room temperature with a P_{ex} value of 5.0 mW and a spectral integration time of 1 s. (B) $I(1000\ cm^{-1})/I(1074\ cm^{-1})$ at various temperatures. The intensity ratios shown in panel B were the average values of the results collected on 10 SiO_2@Ag SNPs at each temperature, and the error bars represented the standard deviations. The values of $I(1000\ cm^{-1})/I(1074\ cm^{-1})$ exhibited a linear relationship to temperature, and the fitting results were shown as a solid orange line in panel B. (C) Representative SERS spectra of TP on individual SiO_2@Ag SNPs prior to laser illumination, after continuous illumination at a P_{ex} value of 5.0 mW for 30 s in water and after continuous illumination at a P_{ex} value of 5.0 W for 30 s in air. (D) Temporal evolution of $I(1000\ cm^{-1})/I(1074\ cm^{-1})$ during continuous laser illumination (λ_{ex} of 785 nm; P_{ex} of 5.0 W) collected from 10 individual TP-coated SiO_2@Ag SNPs in water (left panel) and in air (right panel). (E) Ensemble-averaged $I(1000\ cm^{-1})/I(1074\ cm^{-1})$ trajectories of TP-coated SiO_2@Ag SNPs during continuous laser illumination at a P_{ex} value of 5.0 mW for 30 s in water and in air. (F) Temporal evolution of the temperatures at the SNP surfaces (calculated based on Raman thermometry) under continuous laser illumination at a P_{ex} value of 5.0 W in water and in air.

quantitatively correlate the reaction kinetics to the local field enhancements.

The non-radiative decay of plasmons gives rise to the formation of short-lived, non-thermal hot carriers that undergo rapid relaxation processes over a broad distribution of time scales ranging from femtoseconds to nanoseconds.[2] These energetic hot carriers can either be transferred to molecular adsorbates to drive photocatalytic reactions or relax into lower energy charge carriers distributed fairly close to the Fermi level of the metals through cascading inelastic electron−electron and electron−surface scattering processes. The resulting lower-energy electrons then get thermalized by coupling with the phonon modes to generate heat, a process known as plasmonic photothermal conversion, which may also kinetically boost molecular transformations on the surfaces of light-illuminated plasmonic nanostructures. However, it has long been challenging to unambiguously delineate the thermal and non-thermal effects involved in plasmon-mediated surface chemistry[20,61−70] largely due to the mechanistic complexity of the plasmon-driven reactions and the challenges associated with precise measurement of the local temperature on the photocatalyst surfaces. Whether a specific plasmon-driven reaction is dominated by the non-thermal or thermal effects has been a subject under intense debate, and it has become increasingly evident that some important conclusions drawn from earlier studies are well worthy of cautious re-examination and further scrutiny.[20,49−57] The power dependence of reaction rates provides important implications that may help us distinguish the photothermal from non-thermal photochemical effects.[6,20,61,65] As shown in Figure 2B, the $I_0(1074\ cm^{-1})$ averaged over all SiO_2@Ag SNPs measured at each P_{ex}, $\langle I_0(1074\ cm^{-1})\rangle$, was directly proportional to P_{ex}, which was fully consistent with eq 5. However, the ensemble-averaged k_{obs} values, $\langle k_{obs}\rangle$, exhibited a superlinear relationship to P_{ex} (Figure 2C). We performed least-squares curve fitting to the experimental data with the following equation

$$\langle k_{obs}\rangle = B \times \left(\frac{P_{ex}}{1\ mW}\right)^n \quad (8)$$

in which $\langle k_{obs}\rangle$ was equal to the nth power of P_{ex} multipled by a scaling coefficient, B. The best fitting result was obtained when n took the value of 1.45. Because of the superlinear

https://doi.org/10.1021/acs.jpcc.1c07177
J. Phys. Chem. C 2021, 125, 20958−20971

power dependence, k_{obs} became more sensitive to the variation of $|E_{Loc}(\omega_L)/E_0(\omega_L)|^4$ as P_{ex} increased, resulting in larger φ values at higher P_{ex} values (Figure 2D).

As evidenced by ample examples in the literature, the rate of a plasmonic hot-carrier-driven reaction is typically proportional to the excitation power under CW illumination at moderate photon power densities.[6,9,19,20,61,71] However, such a linear power dependence may switch to a superlinear power dependence when reaching a sufficiently high power density regime or under ultrafast pulsed laser illumination as a consequence of multiphoton absorption. Therefore, the transition from the linear to the superlinear power dependence over a certain power density regime has been considered as a hallmark of hot-carrier-driven photocatalysis.[6,9,19,20,61,71] However, the non-linearity of power dependence may also originate solely from the photothermal heating without the involvement of the hot carriers.[61] For a photothermally activated reaction, the rate constant typically obeys the Arrhenius-type temperature dependence.[61,62] Assuming that the temperature elevation due to light absorption was approximately proportional to the incident power impinging on the sample surfaces under our experimental conditions, the relationship between k_{obs} and P_{ex} could be expressed by the following equation

$$k_{obs} = A \times e^{-E_a/R(T_0+cP_{ex})} \quad (9)$$

where A was the pre-exponential factor, E_a was the activation energy, R was the gas constant, T_0 was the initial temperature before light illumination (295 K in our case), and c was a scaling factor relating the temperature elevation to the illumination power. The experimental results shown in Figure 2C could be fitted almost equally well with eqs 8 and 9 (Figure S9 in the Supporting Information), and it was highly likely that the observed power dependence reflected a superposition of thermal and non-thermal components.

To gain further insight into the relative contributions of the non-thermal hot carriers vs photothermal heating, we first conducted an important control experiment, in which the 4-MBA-coated SiO_2@Ag SNPs were exposed to an aqueous solution of 1.0 mM K_2CO_3 maintained at 90 °C for 30 min without laser illumination. After the thermal treatment, SERS spectra were collected on individual SNPs at room temperature. As shown in Figure S10 in the Supporting Information, all of the SERS features of 4-mercaptobenzoate were well-preserved without any detectable SERS peaks of TP, indicating that the decarboxylation of 4-mercaptobenzoate was essentially a hot-carrier-driven photoreaction rather than a thermally activated reaction. Next, we scrutinized the rationality of the E_a and c values obtained from the curve fitting. Fitting the experimental results with eq 9 yielded an E_a value of 15.4 ± 0.94 kJ mol^{-1}, which appeared too low for a reaction involving the cleavage of a C−C covalent bond under thermal conditions. With a c value of 146 ± 39 K mW^{-1}, the temperature at the photocatalyst surfaces under laser illumination at a P_{ex} value of 5.0 mW would exceed 1000 K, at which the melting of Ag nanoparticles and thermal decomposition of the organic adsorbates were both expected to occur but neither was observed experimentally. Therefore, although the experimental results could be well-fitted with the Arrhenius-type power dependence, this decarboxylation reaction was unlikely to be driven solely by photothermal heating. Last and most importantly, we further developed a semi-quantitative Raman thermometry to probe the local temperature at the photocatalyst surfaces, based upon which we were able to directly evaluate the contribution of photothermal heating.

TP chemisorbed to the SiO_2@Ag SNPs exhibited unique temperature-dependent SERS features, which enabled us to use TP as a probe molecule for the Raman thermometry. Upon thermal heating of the TP-coated SiO_2@Ag SNPs to higher temperatures, both $I(1000\ cm^{-1})/I(1074\ cm^{-1})$ and $I(1022\ cm^{-1})/I(1074\ cm^{-1})$ decreased and the ν(CS) mode slightly down-shifted (Figure 3A). These spectral changes caused by thermal treatment were found to be irreversible, all of which were well-preserved after the samples were cooled down to room temperature. Such thermally induced changes in the SERS spectra of TP were also previously observed on other nanostructured Ag surfaces,[58,72] which were caused by conformational changes of the surface-adsorbed TP, as suggested by DFT calculations.[58] The values of $I(1000\ cm^{-1})/I(1074\ cm^{-1})$ varied linearly with respect to temperature changes (Figure 3B), providing a working curve for us to calculate the local surface temperatures in the plasmonic hot spots where the TP molecules resided.

The SERS spectra of individual TP-coated SiO_2@Ag SNPs after exposure to continuous laser illumination at a P_{ex} value of 5.0 mW (the maximal P_{ex} investigated in this work) revealed remarkably different temperature elevation profiles in H_2O and in air (Figure 3C and D). Upon laser illumination, the surface temperature of the SNPs gradually increased, reaching a steady state value when the equilibrium between heat generation and dissipation was established after approximately 15 s. When the SiO_2@Ag SNPs were exposed to air, their surface temperature increased from 22 to ∼75 °C after laser illumination for 30 s, whereas a limited temperature elevation by only ∼13 °C was achieved on SNPs exposed to H_2O (Figure 3E and F). Therefore, the plasmonic heating effects were rather insignificant during the plasmon-driven decarboxylation reactions. The steady state values of $I(1000\ cm^{-1})/I(1074\ cm^{-1})$ in the SERS spectra of TP on SiO_2@Ag SNPs under continuous laser illuminations remained around 1 over the entire laser power range we investigated, dropping slightly from ∼1.03 at a P_{ex} value of 0.32 mW to ∼0.97 at a P_{ex} value of 5.0 mW. Although the photothermal transduction efficiency was an intrinsic property of the SNPs themselves, the steady state surface temperatures of the laser-illuminated SNPs also critically depended upon heat dissipation, which was influenced by the thermal conductivity of the local medium surrounding the SNPs.[61,73,74] Significantly higher temperature elevation was observed on SNPs in air than those in H_2O because the thermal conductivity of H_2O (∼0.6 W m^{-1} K^{-1}) was more than 20 times higher than that of air (0.025 W m^{-1} K^{-1}). We also studied the temperature dependence of the decarboxylation rates under laser illumination at a P_{ex} value of 0.32 mW using a heating plate in contact with the Si substrates to control the bulk reaction temperatures. At such a low P_{ex}, the plasmonic photothermal heating effect became negligible and we assumed that temperatures of the medium in the reaction chambers were well-maintained around the targeted temperatures. When raising the reaction temperature from 22 to 40 °C, the reaction rates and yields only slightly increased by less than 10% (Figure S11 in the Supporting Information), further verifying the insignificant contribution of photothermal heating to the kinetic enhancement even at P_{ex} values up to 5.0 mW. Therefore, the observed non-linear power dependence of k_{obs} was mostly like a characteristic of a hot-carrier-driven

https://doi.org/10.1021/acs.jpcc.1c07177
J. Phys. Chem. C 2021, 125, 20958−20971

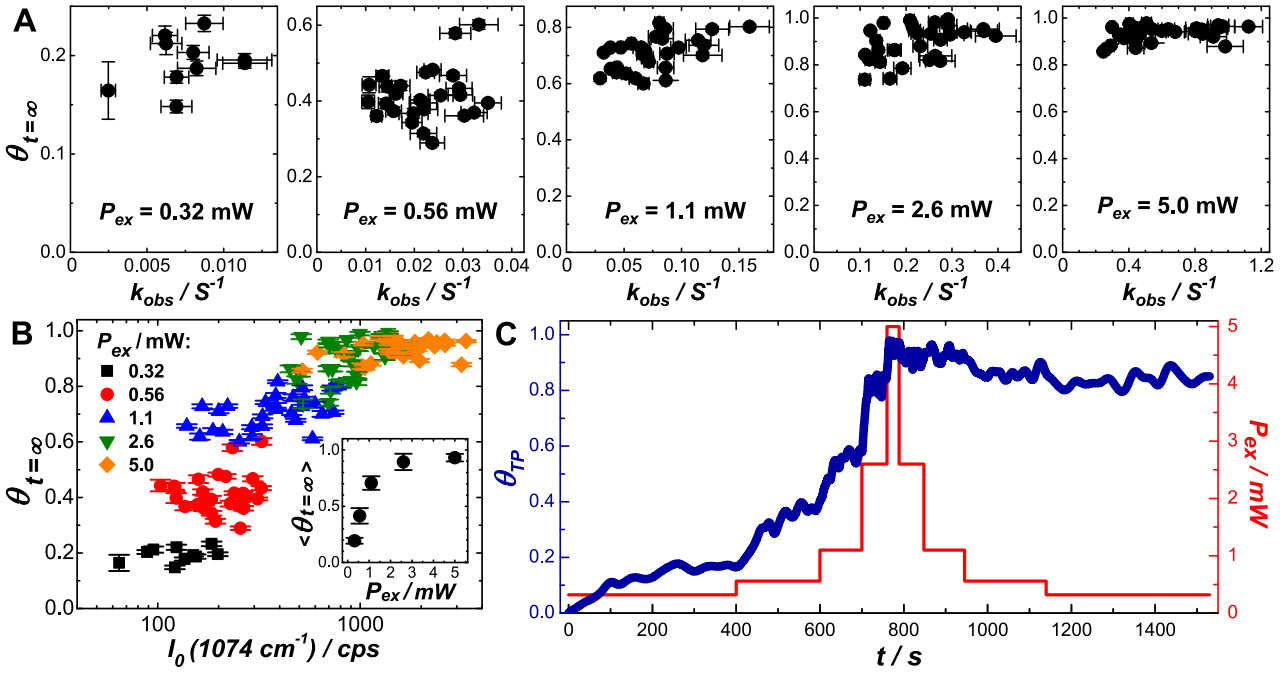

Figure 4. (A) Relationship between $\theta_{t=\infty}$ and k_{obs}. (B) Plots of $\theta_{t=\infty}$ vs $I_0(1074\ cm^{-1})$ at five different P_{ex} values of 0.32, 0.56, 1.1, 2.6, and 5.0 mW. At each P_{ex}, the time-resolved SERS measurements were collected on different individual SiO_2@Ag NC SNPs one particle at a time. The inset of panel B shows ensemble-averaged $\theta_{t=\infty}$ as a function of P_{ex}. The error bars in panels A and B represent the standard deviations of the curve-fitting results. (C) Temporal evolution of θ_{TP} (navy blue) during the decarboxylation reactions under continuous laser illumination with programmed P_{ex} (red).

reaction involving multiphoton absorption rather than a photothermally activated reaction. Although the total excitation powers incident on the samples were in the range of sub-mW to mW, the photon power densities in the focal point (~2 μm in diameter) of the confocal laser beam were as high as several tens of kW cm^{-2}, far exceeding those of the light sources typically used for plasmon-driven photocatalysis.[6,19−21,61,67,68] Because of the high local power densities and intense local-field enhancements, it was not surprising that multiphoton processes became pronounced even under CW laser illumination at mW-level P_{ex} values.

In the SERS measurements, we probed the transforming behaviors of molecular adsorbates residing in the plasmonic hot spots rather than all molecules on the photocatalyst surfaces. Because the reaction rates were sensitively dependent on the local-field enhancements, the decarboxylation reactions occurred regioselectively in the nanoscale hot spots, whereas the molecules in the "electromagnetically cold" surface regions remained unreacted. Therefore, the values of $\theta_{t=\infty}$ extracted from the SERS results represented the apparent reaction yields of the molecules in the hot spots. Even so, not all 4-mercaptobenzoate molecules in the hot spots got decarboxylated within the time duration of our kinetic measurements (Figure S7 in the Supporting Information), resulting in non-unity values of $\theta_{t=\infty}$. Although k_{obs} varied significantly from particle to particle due to the variation in average field enhancements among the SNPs, $\theta_{t=\infty}$ was uncorrelated to k_{obs} at the single SNP level, exhibiting very similar values at a given P_{ex} (Figure 4A). $\theta_{t=\infty}$ appeared almost independent of $I_0(1074\ cm^{-1})$ at each P_{ex} (Figure 4B), while the ensemble-averaged $\theta_{t=\infty}$, $\langle\theta_{t=\infty}\rangle$, increased with P_{ex}, reaching more than 90% yields at a P_{ex} value of 5.0 mW (inset of Figure 4B).

At first glance, the non-unity $\theta_{t=\infty}$ values, especially those observed at low P_{ex} values, could be possibly interpreted in the context of reversible decarboxylation/carboxylation processes under laser illumination. Increasing P_{ex} selectively boosted the decarboxylation of 4-mecarptobenzoate with respect to the carboxylation of TP, thereby shifting the equilibrium toward TP. However, lack of correlation between $\theta_{t=\infty}$ and k_{obs} strongly suggested that the non-unity $\theta_{t=\infty}$ values were unlikely to be a consequence of dynamic equilibrium between decarboxylation and carboxylation. To gain further insights into the reaction reversibility, we carried out P_{ex}-programmed kinetic measurements, in which the 4-MBA-coated SiO_2@Ag SNPs were exposed to 1.0 mM K_2CO_3 under continuous illumination by 785 nm laser at varying P_{ex}. As shown in Figure 4C, we started with a low P_{ex} value at 0.32 mW and then progressively increased P_{ex} to 5.0 mW in a stepwise manner. At each P_{ex}, we collected the SERS spectra continuously until θ_{TP} reached a plateau. Every time we increased P_{ex}, a higher fraction of TP was produced and $\theta_{t=\infty}$ increased until exceeding 90% at a P_{ex} value of 5.0 mW. Upon a decrease in P_{ex}, no reserve reaction was observed within the time windows of our measurements, and $\theta_{t=\infty}$ remained above 80% even at a P_{ex} value as low as 0.32 mW. The results of P_{ex}-programmed SERS measurements strongly indicated that the plasmon-driven decarboxylation reaction was an irreversible process. We hypothesized that the molecules became activated for the photocatalytic decarboxylation only when the local-field intensities ($|E_{Loc}(\omega_L)|$) at the molecule-occupying sites exceeded a certain threshold value, whereas the molecules remained unreactive when residing in the colder regions where $|E_{Loc}(\omega_L)|$ was below the threshold value. Although the average field enhancements, $|E_{Loc}(\omega_L)/E_0(\omega_L)|$, in each SNP varied from particle to particle, the threshold $|E_{Loc}(\omega_L)|$ value required for the molecular activation stayed essentially the same for all SNPs at all P_{ex} values. An increase in P_{ex} resulted in higher fractions of the molecules occupying the surface sites

https://doi.org/10.1021/acs.jpcc.1c07177
J. Phys. Chem. C 2021, 125, 20958−20971

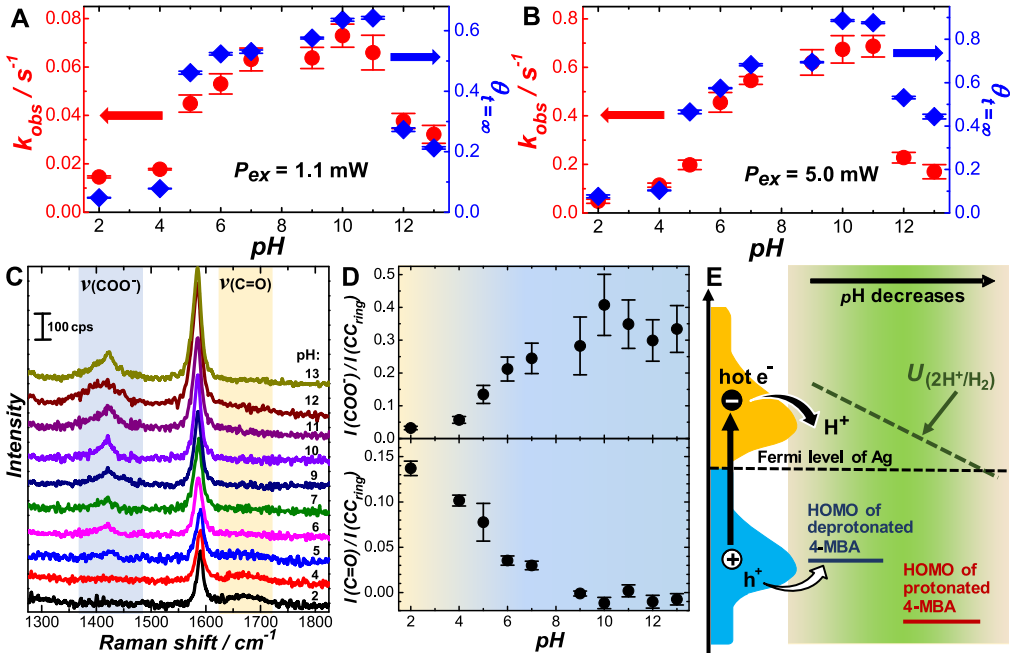

Figure 5. Ensemble-averaged k_{obs} (red circles) and $\theta_{t=\infty}$ (blue diamonds) as a function of pH values at P_{ex} values of (A) 1.1 and (B) 5.0 mW. (C) pH-dependent SERS spectra of 4-MBA adsorbed on SiO_2@Ag NC SNPs. (D) Evolution of the intensity ratios of (upper panel) $I(COO^-)/I(CC_{ring})$ and (lower panel) $I(C{=}O)/I(CC_{ring})$ as the pH varies. (E) Energy diagram illustrating the plasmonic hot carrier transfers involved in the decarboxylation of 4-MBA chemisorbed on Ag at various pHs.

with $|E_{Loc}(\omega_L)|$ above the threshold value, giving rise to increased $\theta_{t=\infty}$. However, how the surface-adsorbed 4-mercaptobenzoate gets activated by the local fields still remains unclear and the exact value of the threshold $|E_{Loc}(\omega_L)|$ still needs to be determined.

Both the rates and the yields of the decarboxylation reactions changed significantly upon variation in the pH of the medium to which the 4-MBA-coated SiO_2@Ag SNPs were exposed, exhibiting an interesting volcano-type pH dependence at P_{ex} values of both 1.1 (Figure 5A and Figure S12 in the Supporting Information) and 5.0 mW (Figure 5B and Figure S13 in the Supporting Information). In this set of experiments, the pH of the reaction medium was adjusted in the range of 2−13 using HCl−NaOH mixtures. At a pH of 10, both the reaction rates and yields remained essentially unchanged when switching from 1.0 mM K_2CO_3 to the HCl−NaOH system (Figures S7F, S12G, and S13G in the Supporting Information). In an acidic environment at a pH below 4, the decarboxylation reactions were observed to be kinetically sluggish with very limited reaction yields below ∼15%. As the pH of the reaction medium went up, both k_{obs} and $\theta_{t=\infty}$ increased remarkably, approaching the maximal values in the pH range of 10−11. It has been previously reported that deprotonated 4-MBA on Ag and Au nanoparticle surfaces underwent decarboxylation reactions upon optical excitation of the nanoparticle plasmons, whereas protonated 4-MBA remained unreactive.[32,36] Upon receiving a plasmonic hot hole from Ag, a surface-adsorbed 4-mercaptobenzoate anion was converted to a carboxyl radical, which readily underwent C—C bond cleavage to release CO_2. A sharp increase of k_{obs} and $\theta_{t=\infty}$ observed over the pH range of 4−7 correlated well with the deprotonation of 4-MBA in this particular pH window, which was further verified by the SERS spectra collected from 4-MBA-coated SiO_2@Ag SNPs at different pHs.

As shown in Figure 5C, the protonated 4-MBA in an acidic environment exhibited a broad SERS peak centered at 1680 cm^{-1}, which was assigned to the C═O vibrational mode, ν(C═O), of the protonated carboxylic acid group.[48−50] Deprotonation of 4-MBA led to the disappearance of the ν(C═O) mode, accompanied by the emergence of the $\nu(COO^-)$ mode of the carboxylate group at 1420 cm^{-1}. The major changes in the SERS spectral features of 4-MBA upon deprotonation/protonation were well-reproduced computationally through DFT calculations of the Raman spectra of 4-MBA covalently linked to Ag atomic clusters (Figure S14 in the Supporting Information). According to the evolution of the relative SERS intensities of the ν(C═O) and $\nu(COO^-)$ modes (Figure 5D), the pK_a of the surface-adsorbed 4-MBA was determined to be around 5, which was consistent with previously reported values.[48−50] Therefore, the pH dependence of k_{obs} and $\theta_{t=\infty}$ was directly tied to the relative fractions of the protonated and deprotonated forms of 4-MBA in the plasmonic hot spots.

To gain further insight into the pH-dependent kinetics and reactivity, we used DFT to calculate the frontier orbital energies of protonated and deprotonated 4-MBA covalently linked to Ag_n clusters (n refers to the number of atoms in the Ag clusters). As shown in Figure S15 in the Supporting Information, the chemisorption of both the protonated and deprotonated 4-MBA to Ag resulted in significant narrowing of the band gaps between the HOMO and the LUMO, shifting both orbitals closer to the Fermi level of Ag. At a λ_{ex} value of 785 nm (1.58 eV), the plasmonic hot electrons were distributed in the energy range within 1.58 eV above the Fermi level, and thus were not energetic enough to get injected into the LUMO of the 4-MBA−Ag_n complexes. Therefore, it was the solution-phase protons rather than the surface-adsorbed 4-MBA or 4-mercaptobenzoate that served as the

https://doi.org/10.1021/acs.jpcc.1c07177
J. Phys. Chem. C 2021, 125, 20958−20971

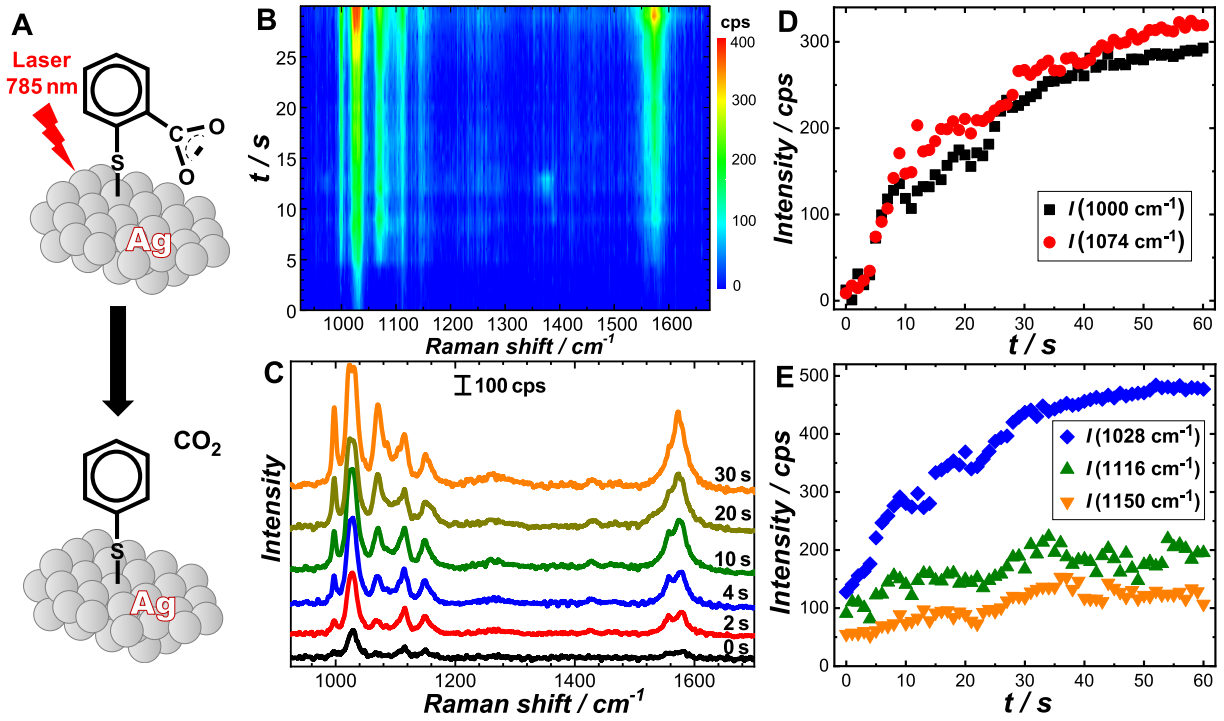

Figure 6. (A) Schematic illustration of the plasmon-driven decarboxylation of 2-MBA chemisorbed on a Ag surface under 785 nm laser illumination. (B) Time-resolved SERS spectra collected on one 2-MBA-coated SiO_2@Ag SNP upon exposure to 1.0 mM K_2CO_3 (pH 10) under 785 nm laser illumination. The spectral acquisition time was 1 s, and the laser power was 2.6 mW. (C) Snapshot SERS spectra collected on one 2-MBA-coated SiO_2@Ag SNP upon exposure to 785 nm laser illumination collected at reaction times of 0, 2, 4, 10, 20, and 30 s. (D) Temporal evolution of $I(1000\ cm^{-1})$ and $I(1074\ cm^{-1})$ obtained from the time-resolved SERS results shown in panel B. (E) Temporal evolution of $I(1028\ cm^{-1})$, $I(1116\ cm^{-1})$, and $I(1150\ cm^{-1})$ obtained from the time-resolved SERS results shown in panel B.

acceptor of hot electrons during the decarboxylation reactions. On the other hand, a fraction of the hot holes (distributed between the Fermi level and 1.58 eV below the Fermi level) had sufficient energy to transfer to the HOMO of the molecular adsorbates. In comparison to those of their protonated counterparts, the HOMOs of deprotonated 4-MBA−Ag_n complexes were further shifted toward the Ag Fermi level. From the band alignment point of view, deprotonation of 4-MBA on Ag was more favorable for the hot hole transfer and the acceleration of decarboxylation reactions than the protonated 4-MBA. According to the DFT-calculated electron density maps of the HOMOs of 4-MBA−Ag_n complexes (Figure S16 in the Supporting Information), deprotonation of the carboxylic acid group resulted in increased electron densities near the Ag_n clusters, making the deprotonated 4-MBA able to more readily accept the hot holes ejected from Ag than the protonated 4-MBA. As a result, the deprotonated 4-MBA was more reactive than the protonated 4-MBA. An alternative possible mechanism of the plasmon-driven decarboxylation of 4-MBA involves the hot-hole-induced oxidation of H_2O into OH• radicals, which then initiate the decarboxylation of the carboxylates.[75] Considering the fact that the redox potentials of H_2O/OH• lie more than 2 eV below the Fermi level of Ag,[76,77] the hot holes are not energetic enough to drive the evolution of OH• from H_2O when the Ag plasmons are excited at 785 nm. Therefore, the plasmon-driven decarboxylation reactions observed under our experimental conditions were essentially induced by hot hole injection into surface-adsorbed 4-mercaptobenzoate rather than being driven by the photogenerated OH• radicals.

Interestingly, we observed a drastic decrease in both k_{obs} and $\theta_{t=\infty}$ in highly basic environments (pH > 11) as the pH further increased (Figure 5A and B), even though all of the surface-adsorbed 4-MBA existed in the deprotonated form. The depletion of hot holes in Ag was compensated by the hot electron injection into protons, which constituted the other half reaction of the redox cycle. The standard redox potential for proton reduction, $U(H^+/H_2)$, at a pH of 0 was 4.5 eV below the vacuum level, which was well aligned with the Fermi level of Ag (4.3 eV below vacuum). $U(H^+/H_2)$ increased as the reaction medium became less acidic, exhibiting a linear dependence on the pH that could be fully described by the classic Nernst equation. In an alkaline environment, $U(H^+/H_2)$ was shifted further above the Ag Fermi level as the pH increased, resulting in a declined population of the hot electrons with sufficient energies to get injected into the protons. As schematically illustrated in Figure 5E, the pH dependence of reaction rates and yields observed in this work could be well-interpreted in the context of the relative energies of the HOMO of the hot hole acceptors and the redox potentials of the hot electron acceptors, both of which could be modulated by varying the pH of the reaction medium.

Analogous to 4-MBA, 2-MBA, when deprotonated, also underwent a decarboxylation reaction to produce TP on the surfaces of laser-illuminated SiO_2@Ag SNPs, as schematically illustrated in Figure 6A. Although a strong peak corresponding to the S−H stretching mode of 2-MBA was observed at around 2530 cm^{-1} in the normal Raman spectrum, it became undetectable in the SERS spectrum (Figure S17 in the Supporting Information), indicating that 2-MBA was chemisorbed to Ag surfaces upon formation of a covalent Ag−S

https://doi.org/10.1021/acs.jpcc.1c07177
J. Phys. Chem. C 2021, 125, 20958−20971

bond rather than physically adsorbed on the Ag surfaces. The strongest peak in the SERS spectrum of deprotonated 2-MBA on SiO_2@Ag SNPs at a pH of 10 was observed to be the ν(C−S) stretching mode centered at 1028 cm^{-1}. The benzene ring mode, $\nu(CC_{ring})$, split into a double-peaked spectral feature (1558 and 1578 cm^{-1}) due to the structural asymmetry of molecules. The calculated Raman spectra of 2-MBA and 2-MBA−Ag_n complexes were in good agreement with the experimentally measured Raman and SERS spectra in terms of the positions of the major peaks (Figure S18 in the Supporting Information); however, the DFT calculations were incapable of precisely predicting the relative intensities of various vibrational modes in the SERS spectra because the simple atomic cluster model we used did not take the surface orientation of the molecule adsorbates and the electromagnetic enhancement effects of SERS into consideration.

Figure 6B shows the time-resolved SERS spectra collected from a 2-MBA-coated SiO_2@Ag SNP exposed to 1.0 mM K_2CO_3 under continuous laser illumination at a P_{ex} value of 2.6 mW. Several snapshot spectra at various reaction stages were highlighted in Figure 6C. As the decarboxylation reaction proceeded, the SERS signatures of TP at 1000 and 1074 cm^{-1} emerged and gradually intensified, while the intensity ratios between the two peaks, I(1000 cm^{-1})/I(1074 cm^{-1}), remained very close to 1 (Figure 6D). The SERS peak of TP at 1022 cm^{-1} spectrally overlapped with the ν(C−S) mode of 2-mercaptobenzoate at 1028 cm^{-1}, giving rise to a double-peaked, broadened spectral feature in the wavenumber range of 1018−1032 cm^{-1} when both the reactant and product molecules coexisted in the plasmonic hot spots. The $\nu(CC_{ring})$ modes of TP and 2-mercaptobenzoate also overlapped at 1578 cm^{-1}. More detailed spectral features in the wavenumber ranges of 975−1175 and 1475−1675 cm^{-1} were highlighted in Figure S19 in the Supporting Information. During the reactions, several characteristic SERS peaks of 2-mercaptobenzoate centered at 1128, 1116, and 1150 cm^{-1} all became remarkably stronger (Figure 6E), while both the peak positions and relative peak intensities remained essentially unchanged. Such intensified SERS signals of 2-mercaptobenzoate might originate from the orientational changes of 2-mercaptobenzoate with respect to the Ag surfaces when some of the adsorbate molecules were converted into TP. How the molecular orientations are influenced by the decarboxylation reactions, however, still needs to be further investigated in greater detail. Although the temporal evolution of SERS spectral features allowed us to track the plasmon-driven decarboxylation process, the intrinsic spectral complexity of 2-mercaptobenzoate, the variation of the SERS intensities, and the spectral overlap between several major SERS peaks kept us from being able to extract the k_{obs} and $\theta_{t=\infty}$ values from the time-resolved SERS results. Therefore, it remains challenging to quantitatively compare the decarboxylation rates of 2-mercaptobenzoate to those of 4-mercaptobenzoate under specific reaction conditions.

The decarboxylation of 2-mercaptobenzoate was verified as a plasmon-driven photochemical reaction rather than a thermally activated process because no reaction was observed under thermal conditions even at temperatures up to 90 °C (Figure S20 in the Supporting Information). Similar to 4-mercaptobenzoate, 2-mercaptobenzoate underwent fast decarboxylation reactions on the surfaces of laser-illuminated SiO_2@Ag SNPs at a pH of 10 but became essentially unreactive at a pH of 2 (Figure S21 in the Supporting Information). In this acidic medium, the intensities of all of the SERS peaks of the protonated 2-MBA remained unchanged under continuous laser illumination, further indicating that the amplification of 2-mercaptobenzoate SERS signals observed at a pH of 10 (Figure 6B and C) was associated with the photochemical decarboxylation reactions rather than being photophysically induced by the laser illumination. Analogous to the case of 4-MBA, the deprotonation of the carboxylic acid group shifted the HOMO of the surface-adsorbed 2-MBA closer to the Ag Fermi level (Figure S22 in the Supporting Information), thereby making the deprotonated form energetically more favorable for the metal-to-adsorbate transfer of hot holes than the protonated form.

CONCLUSIONS

The plasmon-driven decarboxylation reactions studied in this work fully demonstrate the feasibility of utilizing optically excited metallic nanostructures as plasmonic molecular scissors for selective cleavage of targeted chemical bonds in molecular adsorbates. Distinct from previously investigated hot-electron-driven bond-breaking processes, the photocatalytic decarboxylation of aromatic carboxylates chemisorbed on Ag surfaces was induced by the transfer of plasmonic hot holes from the metal to the molecular adsorbates, while the protons in close proximity to the metal−solution interfaces served as the hot electron acceptors. Using SERS as an *in situ* plasmon-enhanced spectroscopic tool enables us not only to precisely resolve the detailed structural evolution of the transforming molecules in the plasmonic hot spots but also to delve into the underlying correlations between the molecule-transforming kinetics and the intrinsic plasmonic properties of the metallic nanophotocatalysts. Through combined experimental and computational efforts, we have been able to gain quantitative insights concerning several pivotal aspects of the perplexing reaction mechanism. (1) The reaction rate is sensitively dependent upon the local-field enhancement at the photocatalyst surface, exhibiting a linear proportionality to the fourth power of the field enhancement. (2) The apparent rate constants exhibit a superlinear power dependence when the excitation power is varied in the range from sub-mW to mW. The non-linearity of the observed power dependence is essentially a hallmark of a hot-carrier-driven reaction involving multiphoton absorption, with negligible contribution from the local photothermal heating at the photocatalyst surfaces under our experimental conditions. (3) The power dependence of the reaction yields strongly suggests the existence of a threshold local-field intensity for the molecular activation. Only the molecular adsorbates occupying the surface sites with local-field intensities greater than the threshold value can be photoactivated for the decarboxylation reactions, whereas the molecules experiencing weaker local fields below the threshold remain essentially unreactive. (4) The frontier orbital energies of the hot hole acceptors and the redox potentials of the hot electron acceptors can both be modulated with respect to the Fermi level of the metal by adjusting the pH of the reaction medium, which gives rise to a volcano-type pH dependence of the reaction kinetics with maximal reaction rates and yields achievable in weakly alkaline media at a pH of 10−11. The plasmonic hot holes can be harnessed not only to induce bond cleavage in molecular adsorbates, as exemplified by this work, but also to drive bond-forming coupling reactions, such as the regioselective click reactions, which was recently demonstrated by Jiang, Wang, and co-workers.[78] The insightful knowledge

https://doi.org/10.1021/acs.jpcc.1c07177
J. Phys. Chem. C 2021, 125, 20958−20971

extracted from this work remarkably enhances our capabilities to rationally tailor both the nanophotocatalyst structures and local reaction environments for specifically targeted reactions, thereby pushing the plasmonic hot-carrier-mediated photochemistry toward a higher level of specificity, precision, and versatility.

■ ASSOCIATED CONTENT

Supporting Information

The Supporting Information is available free of charge at https://pubs.acs.org/doi/10.1021/acs.jpcc.1c07177.

Additional experimental details and additional figures including SEM images, TEM images, optical microscopy images, optical extinction spectra, SERS spectra, DFT results, and detailed kinetic results as noted in the text (PDF)

■ AUTHOR INFORMATION

Corresponding Author

Hui Wang − *Department of Chemistry and Biochemistry, University of South Carolina, Columbia, South Carolina 29208, United States;* orcid.org/0000-0002-1874-5137; Phone: 803-777-2203; Email: wang344@mailbox.sc.edu; Fax: 803-777-9521

Authors

Qingfeng Zhang − *Department of Chemistry and Biochemistry, University of South Carolina, Columbia, South Carolina 29208, United States;* Present Address: College of Chemistry and Molecular Sciences, Wuhan University, Wuhan, Hubei 430072, China; orcid.org/0000-0002-7004-9040

Kexun Chen − *Department of Chemistry and Biochemistry, University of South Carolina, Columbia, South Carolina 29208, United States*

Complete contact information is available at: https://pubs.acs.org/10.1021/acs.jpcc.1c07177

Author Contributions

Q.Z. and H.W. conceived the idea. Q.Z. and K.C. collected the experimental data. K.C. did the DFT calculations. Q.Z., K.C, and H.W. analyzed the data. H.W. designed the project, supervised the research, acquired funding support, and wrote the paper with contribution from all authors. All authors have given approval to the final version of the manuscript.

Notes

The authors declare no competing financial interest.

■ ACKNOWLEDGMENTS

This work was supported by the National Science Foundation through award OIA-1655740 and by the University of South Carolina (UofSC) Office of Vice President for Research through an ASPIRE-I Track-IV Award. Q.Z. was partially supported by a UofSC NanoCenter Dissertation Fellowship. The authors would like to thank Prof. Vitaly Rassolov of UofSC for insightful discussions regarding the DFT calculations. This work made use of the facilities at the UofSC Electron Microscopy Center and W.M. Keck Open Laboratory.

■ REFERENCES

(1) Baffou, G.; Quidant, R. Nanoplasmonics for Chemistry. *Chem. Soc. Rev.* **2014**, *43*, 3898−3907.

(2) Brongersma, M. L.; Halas, N. J.; Nordlander, P. Plasmon-Induced Hot Carrier Science and Technology. *Nat. Nanotechnol.* **2015**, *10*, 25−34.

(3) Chen, K. X.; Wang, H. Plasmon-Driven Photocatalytic Molecular Transformations on Metallic Nanostructure Surfaces: Mechanistic Insights Gained from Plasmon-Enhanced Raman Spectroscopy. *Mol. Syst. Des. Eng.* **2021**, *6*, 250−280.

(4) Christopher, P.; Moskovits, M.; Johnson, M. A.; Martinez, T. J. Hot Charge Carrier Transmission from Plasmonic Nanostructures. *Annu. Rev. Phys. Chem.* **2017**, *68*, 379−398.

(5) Gelle, A.; Jin, T.; de la Garza, L.; Price, G. D.; Besteiro, L. V.; Moores, A. Applications of Plasmon-Enhanced Nanocatalysis to Organic Transformations. *Chem. Rev.* **2020**, *120*, 986−1041.

(6) Kale, M. J.; Avanesian, T.; Christopher, P. Direct Photocatalysis by Plasmonic Nanostructures. *ACS Catal.* **2014**, *4*, 116−128.

(7) Kazuma, E.; Kim, Y. Mechanistic Studies of Plasmon Chemistry on Metal Catalysts. *Angew. Chem., Int. Ed.* **2019**, *58*, 4800−4808.

(8) Kherbouche, I.; Luo, Y.; Felidj, N.; Mangeney, C. Plasmon-Mediated Surface Functionalization: New Horizons for the Control of Surface Chemistry on the Nanoscale. *Chem. Mater.* **2020**, *32*, 5442−5454.

(9) Linic, S.; Aslam, U.; Boerigter, C.; Morabito, M. Photochemical Transformations on Plasmonic Metal Nanoparticles. *Nat. Mater.* **2015**, *14*, 567−576.

(10) Zhang, Y. C.; He, S.; Guo, W. X.; Hu, Y.; Huang, J. W.; Mulcahy, J. R.; Wei, W. D. Surface-Plasmon-Driven Hot Electron Photochemistry. *Chem. Rev.* **2018**, *118*, 2927−2954.

(11) Zhang, Z. L.; Zhang, C. Y.; Zheng, H. R.; Xu, H. X. Plasmon-Driven Catalysis on Molecules and Nanomaterials. *Acc. Chem. Res.* **2019**, *52*, 2506−2515.

(12) Zhan, C.; Chen, X. J.; Huang, Y. F.; Wu, D. Y.; Tian, Z. Q. Plasmon-Mediated Chemical Reactions on Nanostructures Unveiled by Surface-Enhanced Raman Spectroscopy. *Acc. Chem. Res.* **2019**, *52*, 2784−2792.

(13) Gargiulo, J.; Berte, R.; Li, Y.; Maier, S. A.; Cortes, E. From Optical to Chemical Hot Spots in Plasmonics. *Acc. Chem. Res.* **2019**, *52*, 2525−2535.

(14) Zhan, C.; Moskovits, M.; Tian, Z. Q. Recent Progress and Prospects in Plasmon-Mediated Chemical Reaction. *Matter* **2020**, *3*, 42−56.

(15) Halas, N. J.; Lal, S.; Chang, W. S.; Link, S.; Nordlander, P. Plasmons in Strongly Coupled Metallic Nanostructures. *Chem. Rev.* **2011**, *111*, 3913−3961.

(16) Jain, P. K.; Huang, X. H.; El-Sayed, I. H.; El-Sayed, M. A. Noble Metals on the Nanoscale: Optical and Photothermal Properties and Some Applications in Imaging, Sensing, Biology, and Medicine. *Acc. Chem. Res.* **2008**, *41*, 1578−1586.

(17) Liz-Marzan, L. M. Tailoring Surface Plasmons through the Morphology and Assembly of Metal Nanoparticles. *Langmuir* **2006**, *22*, 32−41.

(18) Ozbay, E. Plasmonics: Merging Photonics and Electronics at Nanoscale Dimensions. *Science* **2006**, *311*, 189−193.

(19) Mukherjee, S.; Libisch, F.; Large, N.; Neumann, O.; Brown, L. V.; Cheng, J.; Lassiter, J. B.; Carter, E. A.; Nordlander, P.; Halas, N. J. Hot Electrons Do the Impossible: Plasmon-Induced Dissociation of H_2 on Au. *Nano Lett.* **2013**, *13*, 240−247.

(20) Zhou, L. A.; Swearer, D. F.; Zhang, C.; Robatjazi, H.; Zhao, H. Q.; Henderson, L.; Dong, L. L.; Christopher, P.; Carter, E. A.; Nordlander, P.; et al. Quantifying Hot Carrier and Thermal Contributions in Plasmonic Photocatalysis. *Science* **2018**, *362*, 69−72.

(21) Christopher, P.; Xin, H. L.; Linic, S. Visible-Light-Enhanced Catalytic Oxidation Reactions on Plasmonic Silver Nanostructures. *Nat. Chem.* **2011**, *3*, 467−472.

(22) Kazuma, E.; Jung, J.; Ueba, H.; Trenary, M.; Kim, Y. Real-Space and Real-Time Observation of a Plasmon-Induced Chemical Reaction of a Single Molecule. *Science* **2018**, *360*, 521−525.

(23) Brooks, J. L.; Chulhai, D. V.; Yu, Z. W.; Goodpaster, J. D.; Frontiera, R. R. Plasmon-Driven C-N Bond Cleavage across a Series of Viologen Derivatives. *J. Phys. Chem. C* **2019**, *123*, 29306−29313.

(24) Tesema, T. E.; Kafle, B.; Tadesse, M. G.; Habteyes, T. G. Plasmon-Enhanced Resonant Excitation and Demethylation of Methylene Blue. *J. Phys. Chem. C* **2017**, *121*, 7421−7428.
(25) Tesema, T. E.; Annesley, C.; Habteyes, T. G. Plasmon-Enhanced Autocatalytic N-Demethylation. *J. Phys. Chem. C* **2018**, *122*, 19831−19841.
(26) Tesema, T. E.; Kafle, B.; Habteyes, T. G. Plasmon-Driven Reaction Mechanisms: Hot Electron Transfer Versus Plasmon-Pumped Adsorbate Excitation. *J. Phys. Chem. C* **2019**, *123*, 8469−8483.
(27) Schurmann, R.; Bald, I. Real-Time Monitoring of Plasmon Induced Dissociative Electron Transfer to the Potential DNA Radiosensitizer 8-Bromoadenine. *Nanoscale* **2017**, *9*, 1951−1955.
(28) Miliutina, E.; Guselnikova, O.; Soldatova, N. S.; Bainova, P.; Elashnikov, R.; Fitl, P.; Kurten, T.; Yusubov, M. S.; Svorcik, V.; Valiev, R. R.; et al. Can Plasmon Change Reaction Path? Decomposition of Unsymmetrical Iodonium Salts as an Organic Probe. *J. Phys. Chem. Lett.* **2020**, *11*, 5770−5776.
(29) Christopher, P.; Xin, H. L.; Marimuthu, A.; Linic, S. Singular Characteristics and Unique Chemical Bond Activation Mechanisms of Photocatalytic Reactions on Plasmonic Nanostructures. *Nat. Mater.* **2012**, *11*, 1044−1050.
(30) Boerigter, C.; Aslam, U.; Linic, S. Mechanism of Charge Transfer from Plasmonic Nanostructures to Chemically Attached Materials. *ACS Nano* **2016**, *10*, 6108−6115.
(31) Boerigter, C.; Campana, R.; Morabito, M.; Linic, S. Evidence and Implications of Direct Charge Excitation as the Dominant Mechanism in Plasmon-Mediated Photocatalysis. *Nat. Commun.* **2016**, *7*, 10545.
(32) Huh, H.; Trinh, H. D.; Lee, D.; Yoon, S. How Does a Plasmon-Induced Hot Charge Carrier Break a C-C Bond? *ACS Appl. Mater. Interfaces* **2019**, *11*, 24715−24724.
(33) Michota, A.; Bukowska, J. Surface-Enhanced Raman Scattering (SERS) of 4-Mercaptobenzoic Acid on Silver and Gold Substrates. *J. Raman Spectrosc.* **2003**, *34*, 21−25.
(34) Wang, Y.; Ji, W.; Sui, H. M.; Kitahama, Y.; Ruan, W. D.; Ozaki, Y.; Zhao, B. Exploring the Effect of Intermolecular H-Bonding: A Study on Charge-Transfer Contribution to Surface-Enhanced Raman Scattering of p-Mercaptobenzoic Acid. *J. Phys. Chem. C* **2014**, *118*, 10191−10197.
(35) Smith, G.; Girardon, J. S.; Paul, J. F.; Berrier, E. Dynamics of a Plasmon-Activated P-Mercaptobenzoic Acid Layer Deposited over Au Nanoparticles Using Time-Resolved Sers. *Phys. Chem. Chem. Phys.* **2016**, *18*, 19567−19573.
(36) Zong, Y.; Guo, Q. H.; Xu, M. M.; Yuan, Y. X.; Gu, R. N.; Yao, J. L. Plasmon-Induced Decarboxylation of Mercaptobenzoic Acid on Nanoparticle Film Monitored by Surface-Enhanced Raman Spectroscopy. *RSC Adv.* **2014**, *4*, 31810−31816.
(37) Chen, X. J.; Cabello, G.; Wu, D. Y.; Tian, Z. Q. Surface-Enhanced Raman Spectroscopy toward Application in Plasmonic Photocatalysis on Metal Nanostructures. *J. Photochem. Photobiol., C* **2014**, *21*, 54−80.
(38) Hess, C. New Advances in Using Raman Spectroscopy for the Characterization of Catalysts and Catalytic Reactions. *Chem. Soc. Rev.* **2021**, *50*, 3519−3564.
(39) Xia, X. H.; Zeng, J.; Oetjen, L. K.; Li, Q. G.; Xia, Y. N. Quantitative Analysis of the Role Played by Poly(vinylpyrrolidone) in Seed-Mediated Growth of Ag Nanocrystals. *J. Am. Chem. Soc.* **2012**, *134*, 1793−1801.
(40) Zhang, Q.; Wang, H. Mechanistic Insights on Plasmon-Driven Photocatalytic Oxidative Coupling of Thiophenol Derivatives: Evidence for Steady-State Photoactivated Oxygen. *J. Phys. Chem. C* **2018**, *122*, 5686−5697.
(41) Malynych, S.; Luzinov, I.; Chumanov, G. Poly(vinyl pyridine) as a Universal Surface Modifier for Immobilization of Nanoparticles. *J. Phys. Chem. B* **2002**, *106*, 1280−1285.
(42) Wang, H.; Halas, N. J. Mesoscopic Au "Meatball" Particles. *Adv. Mater.* **2008**, *20*, 820−825.
(43) Wang, H.; Musier-Forsyth, K.; Falk, C.; Barbara, P. F. Single-Molecule Spectroscopic Study of Dynamic Nanoscale DNA Bending Behavior of HIV-1 Nucleocapsid Protein. *J. Phys. Chem. B* **2013**, *117*, 4183−4196.
(44) Keresztury, G.; Holly, S.; Besenyei, G.; Varga, J.; Wang, A. Y.; Durig, J. R. Vibrational-Spectra of Monothiocarbamates. 2. IR and RamanSpectra, Vibrational Assignment, ConformationalAnalysis and Ab-Initio Calculations of S-Methyl-N, N-Dimethylthiocarbamate. *Spectrochim. Acta, Part A* **1993**, *49*, 2007−2026.
(45) Polavarapu, P. L. Abinitio Vibrational Raman and Raman Optical-Activity Spectra. *J. Phys. Chem.* **1990**, *94*, 8106−8112.
(46) Huynh, L. T. M.; Trinh, H. D.; Lee, S.; Yoon, S. Plasmon-Driven Protodeboronation Reactions in Nanogaps. *Nanoscale* **2020**, *12*, 24062−24069.
(47) Zhang, Z. L.; Deckert-Gaudig, T.; Singh, P.; Deckert, V. Single Molecule Level Plasmonic Catalysis - a Dilution Study of P-Nitrothiophenol on Gold Dimers. *Chem. Commun.* **2015**, *51*, 3069−3072.
(48) Bishnoi, S. W.; Rozell, C. J.; Levin, C. S.; Gheith, M. K.; Johnson, B. R.; Johnson, D. H.; Halas, N. J. All-Optical Nanoscale pH Meter. *Nano Lett.* **2006**, *6*, 1687−1692.
(49) Talley, C. E.; Jusinski, L.; Hollars, C. W.; Lane, S. M.; Huser, T. Intracellular pH Sensors Based on Surface-Enhanced Raman Scattering. *Anal. Chem.* **2004**, *76*, 7064−7068.
(50) Wang, F. L.; Widejko, R. G.; Yang, Z. Q.; Nguyen, K. T.; Chen, H. Y.; Fernando, L. P.; Christensen, K. A.; Anker, J. N. Surface-Enhanced Raman Scattering Detection of pH with Silica-Encapsulated 4-Mercaptobenzoic Acid-Functionalized Silver Nanoparticles. *Anal. Chem.* **2012**, *84*, 8013−8019.
(51) Govorov, A. O.; Zhang, H.; Demir, H. V.; Gun'ko, Y. K. Photogeneration of Hot Plasmonic Electrons with Metal Nanocrystals: Quantum Description and Potential Applications. *Nano Today* **2014**, *9*, 85−101.
(52) Khurgin, J. B. Hot Carriers Generated by Plasmons: Where Are They Generated and Where Do They Go from There? *Faraday Discuss.* **2019**, *214*, 35−58.
(53) Pilot, R.; Signorini, R.; Durante, C.; Orian, L.; Bhamidipati, M.; Fabris, L. A Review on Surface-Enhanced Raman Scattering. *Biosensors* **2019**, *9*, 57.
(54) Ding, S. Y.; You, E. M.; Tian, Z. Q.; Moskovits, M. Electromagnetic Theories of Surface-Enhanced Raman Spectroscopy. *Chem. Soc. Rev.* **2017**, *46*, 4042−4076.
(55) Brooks, J. L.; Frontiera, R. R. Competition between Reaction and Degradation Pathways in Plasmon-Driven Photochemistry. *J. Phys. Chem. C* **2016**, *120*, 20869−20876.
(56) Golubev, A. A.; Khlebtsov, B. N.; Rodriguez, R. D.; Chen, Y.; Zahn, D. R. T. Plasmonic Heating Plays a Dominant Role in the Plasmon-Induced Photocatalytic Reduction of 4-Nitrobenzenethiol. *J. Phys. Chem. C* **2018**, *122*, 5657−5663.
(57) Koopman, W.; Sarhan, R. M.; Stete, F.; Schmitt, C. N. Z.; Bargheer, M. Decoding the Kinetic Limitations of Plasmon Catalysis: The Case of 4-Nitrothiophenol Dimerization. *Nanoscale* **2020**, *12*, 24411−24418.
(58) Zhang, Q. F.; Zhou, Y. D.; Fu, X. Q.; Villarreal, E.; Sun, L. C.; Zou, S. L.; Wang, H. Photothermal Effect, Local Field Dependence, and Charge Carrier Relaying Species in Plasmon-Driven Photocatalysis: A Case Study of Aerobic Nitrothiophenol Coupling Reaction. *J. Phys. Chem. C* **2019**, *123*, 26695−26704.
(59) Seemala, B.; Therrien, A. J.; Lou, M.; Li, K.; Finzel, J. P.; Qi, J.; Nordlander, P.; Christopher, P. Plasmon-Mediated Catalytic O_2 Dissociation on Ag Nanostructures: Hot Electrons or near Fields? *ACS Energy Lett.* **2019**, *4*, 1803−1809.
(60) Hamans, R. F.; Parente, M.; Baldi, A. Super-Resolution Mapping of a Chemical Reaction Driven by Plasmonic Near-Fields. *Nano Lett.* **2021**, *21*, 2149−2155.
(61) Baffou, G.; Bordacchini, I.; Baldi, A.; Quidant, R. Simple Experimental Procedures to Distinguish Photothermal from Hot-Carrier Processes in Plasmonics. *Light: Sci. Appl.* **2020**, *9*, 108.

https://doi.org/10.1021/acs.jpcc.1c07177
J. Phys. Chem. C 2021, 125, 20958−20971

(62) Dubi, Y.; Sivan, Y. Hot" Electrons in Metallic Nanostructures-Non-Thermal Carriers or Heating? *Light: Sci. Appl.* **2019**, *8*, 89.
(63) Dubi, Y.; Un, I. W.; Sivan, Y. Thermal Effects - an Alternative Mechanism for Plasmon-Assisted Photocatalysis. *Chem. Sci.* **2020**, *11*, 5017−5027.
(64) Sivan, Y.; Baraban, J.; Un, I. W.; Dubi, Y. Comment on "Quantifying Hot Carrier and Thermal Contributions in Plasmonic Photocatalysis. *Science* **2019**, *364*, No. eaaw9367.
(65) Sivan, Y.; Baraban, J. H.; Dubi, Y. Experimental Practices Required to Isolate Thermal Effects in Plasmonic Photo-Catalysis: Lessons from Recent Experiments. *OSA Continuum* **2020**, *3*, 483−497.
(66) Cortes, E.; Besteiro, L. V.; Alabastri, A.; Baldi, A.; Tagliabue, G.; Demetriadou, A.; Narang, P. Challenges in Plasmonic Catalysis. *ACS Nano* **2020**, *14*, 16202−16219.
(67) Li, X. Q.; Everitt, H. O.; Liu, J. Synergy between Thermal and Nonthermal Effects in Plasmonic Photocatalysis. *Nano Res.* **2020**, *13*, 1268−1280.
(68) Zhang, X.; Li, X. Q.; Reish, M. E.; Zhang, D.; Su, N. Q.; Gutierrez, Y.; Moreno, F.; Yang, W. T.; Everitt, H. O.; Liu, J. Plasmon-Enhanced Catalysis: Distinguishing Thermal and Non-thermal Effects. *Nano Lett.* **2018**, *18*, 1714−1723.
(69) Keller, E. L.; Frontiera, R. R. Ultrafast Nanoscale Raman Thermometry Proves Heating Is Not a Primary Mechanism for Plasmon-Driven Photocatalysis. *ACS Nano* **2018**, *12*, 5848−5855.
(70) Zhan, C.; Liu, B. W.; Huang, Y. F.; Hu, S.; Ren, B.; Moskovits, M.; Tian, Z. Q. Disentangling Charge Carrier from Photothermal Effects in Plasmonic Metal Nanostructures. *Nat. Commun.* **2019**, *10*, 2671.
(71) Swearer, D. F.; Zhao, H. Q.; Zhou, L. N.; Zhang, C.; Robatjazi, H.; Martirez, J. M. P.; Krauter, C. M.; Yazdi, S.; McClain, M. J.; Ringe, E.; et al. Heterometallic Antenna-Reactor Complexes for Photocatalysis. *Proc. Natl. Acad. Sci. U. S. A.* **2016**, *113*, 8916−8920.
(72) Aggarwal, R. L.; Farrar, L. W.; Saikin, S. K. Increase of SERS Signal Upon Heating or Exposure to a High-Intensity Laser Field: Benzenethiol on an Agfon Substrate. *J. Phys. Chem. C* **2012**, *116*, 16656−16659.
(73) Jain, P. K. Taking the Heat Off of Plasmonic Chemistry. *J. Phys. Chem. C* **2019**, *123*, 24347−24351.
(74) Sarhan, R. M.; Koopman, W.; Schuetz, R.; Schmid, T.; Liebig, F.; Koetz, J.; Bargheer, M. The Importance of Plasmonic Heating for the Plasmon-Driven Photodimerization of 4-Nitrothiophenol. *Sci. Rep.* **2019**, *9*, 3060.
(75) Huang, S.-C.; Wang, X.; Zhao, Q.-Q.; Zhu, J.-F.; Li, C.-W.; He, Y.-H.; Hu, S.; Sartin, M. M.; Yan, S.; Ren, B. Probing Nanoscale Spatial Distribution of Plasmonically Excited Hot Carriers. *Nat. Commun.* **2020**, *11*, 4211.
(76) Donat, F.; Corbel, S.; Alem, H.; Pontvianne, S.; Balan, L.; Medjahdi, G.; Schneider, R. ZnO Nanoparticles Sensitized by $CuInZn_xS_{2+x}$Quantum Dots as Highly Efficient Solar Light Driven Photocatalysts. *Beilstein J. Nanotechnol.* **2017**, *8*, 1080−1093.
(77) Fu, X.; Li, G. G.; Villarreal, E.; Wang, H. Hot Carriers in Action: Multimodal Photocatalysis on Au@SnO_2 Core−Shell Nanoparticles. *Nanoscale* **2019**, *11*, 7324−7334.
(78) Zhang, S.; Yi, W.; Guo, Y.; Jiang, R.; Chen, X.-L.; Yang, B.; Wang, J. Driving Click Reactions with Plasmonic Hot Holes on (Au Core)@(Cu_2O Shell) Nanostructures for Regioselective Production of 1,2,3-Triazoles. *ACS Appl. Nano Mater.* **2021**, *4*, 4623−4631.

https://doi.org/10.1021/acs.jpcc.1c07177
J. Phys. Chem. C 2021, 125, 20958−20971

Supporting Information for

Hot-Hole-Induced Molecular Scissoring: A Case Study of Plasmon-Driven Decarboxylation of Aromatic Carboxylates

Qingfeng Zhang,[†] *Kexun Chen, and Hui Wang**

Department of Chemistry and Biochemistry, University of South Carolina, 631 Sumter Street, Columbia, South Carolina 29208, United States

[*] *To whom correspondence should be addressed.*
Email: wang344@mailbox.sc.edu (H. Wang); Phone: 803-777-2203; Fax: 803-777-9521

Present Address:
[†] *College of Chemistry and Molecular Sciences, Wuhan University, Wuhan, Hubei 430072, China*

S1. Additional Experimental Details

S1.1 Chemicals and Materials

Ethylene glycol (EG) was obtained from VWR International. Polyvinylpyrrolidone (PVP58, MW = ~58,000), thiophenol (C_6H_6S, TP, 99+%), 4-mercaptobenzoic acid ($C_7H_6O_2S$, 4-MBA, 99%), and 2-mercaptobenzoic acid ($C_7H_6O_2S$, 2-MBA, 97%) were purchased from Alfa Aesar. Silver trifluoroacetate (CF_3COOAg, ≥ 99.99%), sodium hydrosulfide hydrate ($NaHS \cdot xH_2O$), hydrochloric acid (HCl, 37% in water), sodium hydroxide solution (NaOH, 50% in water), poly(diallyl dimethylammonium chloride) (PDDA, 20 wt.% in water, MW = 200,000-350,000), and poly-4-vinylpyridine (MW = ~ 60,000) were purchased from Sigma-Aldrich. Carboxylate-functionalized SiO_2 beads with an average diameter of ~1 μm were purchased from Bangs Laboratories, Inc.. Hydrogen peroxide (H_2O_2, 30 %), sulfuric acid (H_2SO_4, 96.10 %), and ethanol (200 proof) were purchased from Fisher Scientific. Acetone was purchased from Honeywell. All reagents were used as received without further purification. Ultrapure water (18.2 MΩ resistivity, Barnstead EasyPure II 7138) was used for all experiments. Silicon wafers were purchased from University Wafers.

S1.2 Synthesis of Ag Nanocubes

Ag nanocubes were synthesized following a protocol developed by Xia and coworkers.[1] In a typical procedure, 20 mL of EG was added into a 100 mL flask and preheated for 40 min under magnetic stir in a temperature-controlled oil bath set at 150 °C. A series of reagents dissolved in EG were sequentially added into the flask using a pipette. Specifically, 0.25 mL of NaHS solution (3 mM) was first added. After 2 min, 1.5 mL of HCl (3 mM) was added, followed by the addition of 5.0 mL of PVP58 (150 mg/mL). After another 2 min, 1.5 mL of CF_3COOAg solution (282 mM) was added. The flask was capped with a glass stopper during the reactions except when the chemical reagents were added. Ag nanocubes with edge-lengths of 36 $\pm$ 0.79 nm were obtained by quenching the reaction with an ice-water bath when the suspension had reached a brown color with a well-defined localized plasmon resonance peak at around 415 nm. After centrifugation and wash with acetone once and water twice, the Ag nanocubes were redispersed in 2 mL of EG as colloidal suspensions for future use.

S1.3 Synthesis of SiO_2@Ag Nanocubes Suprananoparticles (SiO_2@Ag SNPs)

The surfaces of the SiO_2 beads were densely decorated with Ag nanocubes to form SiO_2@Ag SNPs following a previously reported protocol.[2,3] Briefly, a colloidal suspension of carboxylate-functionalized SiO_2 beads (9.8 mg mL^{-1}, suspended in water) was added to 1 mL of aqueous PDDA solution (1%). After sonication for 30 min, the PDDA-functionalized SiO_2 beads were collected by centrifugation and washed three times with pure water. 0.1 mL of the as-synthesized Ag nanocubes was incubated with the colloidal PDDA-functionalized SiO_2 beads under magnetic stir at room temperature for 1 h. The product was centrifuged and then incubated with Ag nanocubes again to increase the surface coverage of Ag nanocubes. This incubation-centrifugation process was repeated five times to achieve a saturated coverage of Ag nanocubes on the surfaces of the PDDA-functionalized SiO_2 beads and the final product was redispersed in water for future use.

S1.4 Structural Characterizations of Nanoparticles

Transmission electron microscopy (TEM) images were obtained using a Hitachi H-8000 transmission electron microscope operated at an accelerating voltage of 200 kV. All samples for TEM measurements were dispersed in water and drop-dried on 300 mesh Formvar/carbon-coated Cu grids. The morphologies of the SiO_2 beads and the SiO_2@Ag SNPs on silicon substrates were also characterized by scanning electron microscopy (SEM) using a Zeiss Ultraplus thermal field emission scanning electron microscope. The optical extinction spectra of the nanoparticles were measured on aqueous colloidal suspensions at room temperature using a Beckman Coulter Du 640 spectrophotometer. Dark-field and bright-field microscopy images were obtained using an Olympus BX51 optical microscope, which was integrated with a BaySpec *Nomadic*^{TM} confocal Raman microscope.

S1.5 Immobilization of Isolated SiO_2@Ag SNPs on Si Substrates

The SERS measurements were performed on individual 4-MAB or 2-MBA-coated SiO_2@Ag SNPs, which were immobilized on poly-4-vinylpyridine-functionalized silicon substrates as a sub-monolayer film of isolated particles.[4-6] In a typical procedure, silicon substrates were cleaned in a piranha solution (H_2SO_4:H_2O_2, 7:3 volume ratio) for 15 min, and then immersed in an ethanolic solution of 1 wt. % poly-4-vinylpyridine for 24 h. The silicon substrates were then thoroughly rinsed with ethanol and dried in a N_2 gas flow before use. The SiO_2@Ag SNPs were incubated with an ethanolic solution of 500 μM 4-MBA or 2-MBA for 4 h, and then washed with ethanol and redispersed in water. The poly-4-vinylpyridine-functionalized silicon substrates were immersed in an aqueous suspension of 4-MBA- or 2-MBA-coated SiO_2@Ag NC SNPs for 1 h. The silicon substrates were thoroughly rinsed with ethanol and dried with N_2 gas after they were removed from the colloidal suspensions of 4-MBA- or 2-MBA-coated SiO_2@Ag SNPs.

S2. Additional Figures

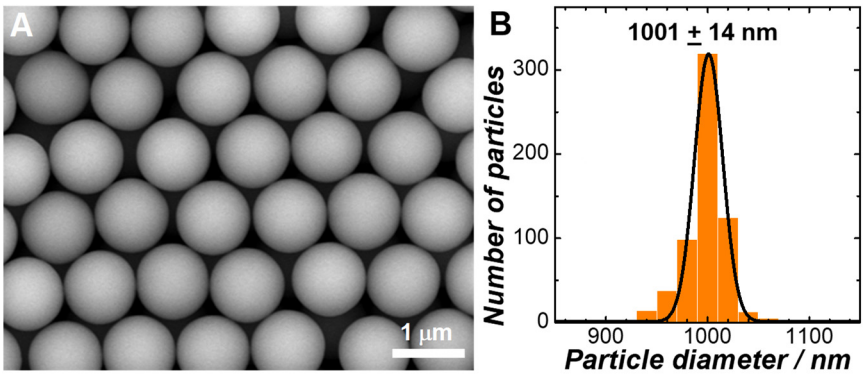

Figure S1. (A) SEM image and (B) size distribution of carboxylate-functionalized SiO_2 beads. The size distribution histograms were fitted with a Gaussian distribution function and the fitting results were shown as the black curve in panel B. The mean particle sizes and standard deviations were also labeled in panel B.

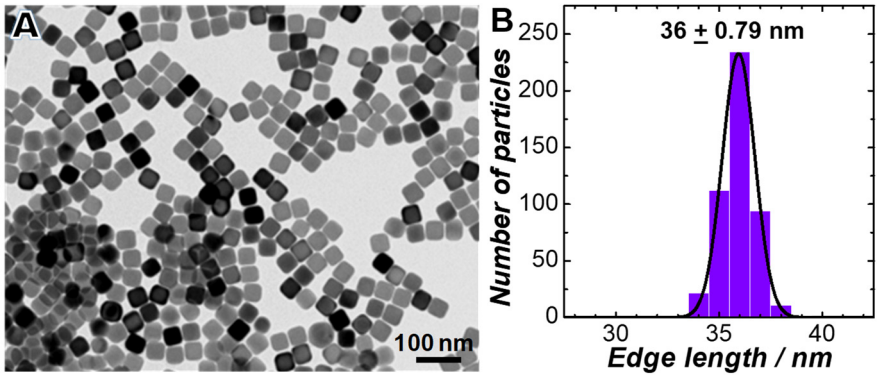

Figure S2. (A) TEM image and (B) size distribution of Ag nanocubes. The size distribution histograms were fitted with a Gaussian distribution function and the fitting results were shown as the black curve in panel B. The mean particle sizes and standard deviations were also labeled in panel B.

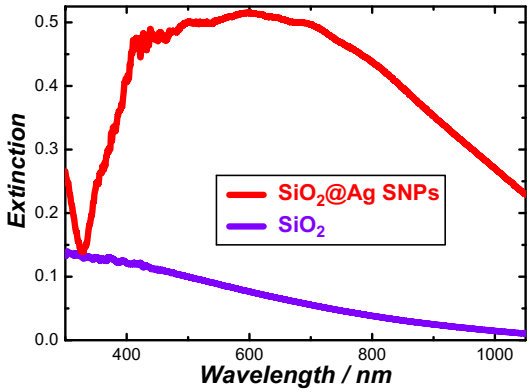

Figure S3. Optical extinction spectra of colloidal carboxylate-functionalized SiO_2 beads and SiO_2@Ag SNPs dispersed in water.

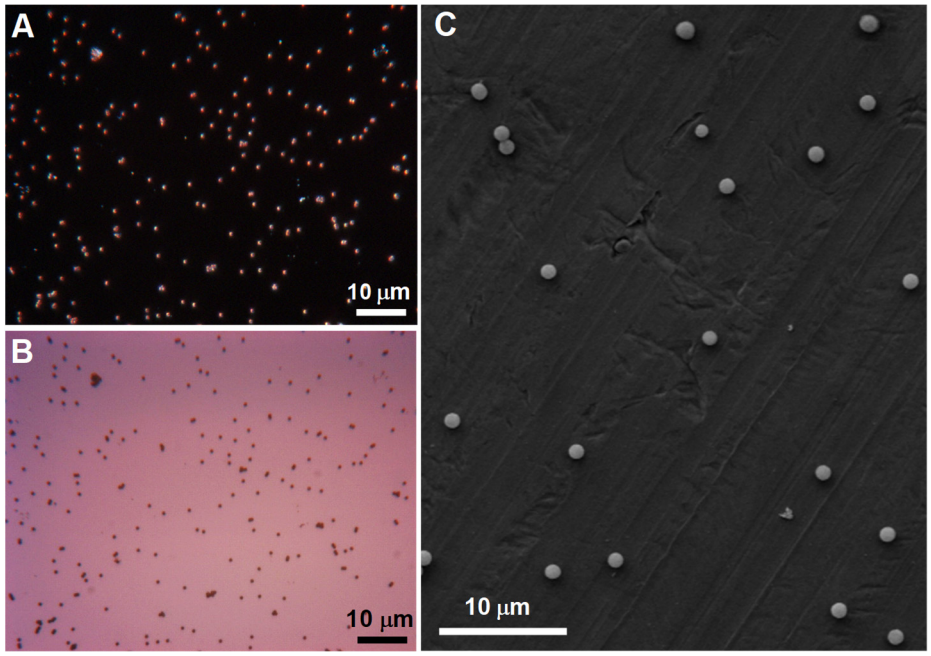

Figure S4. (A) Dark-field optical image, (B) bright-field optical image, and (C) SEM image of isolated SiO_2@Ag SNPs on a poly-4-vinylpyridine-functionalized silicon substrate.

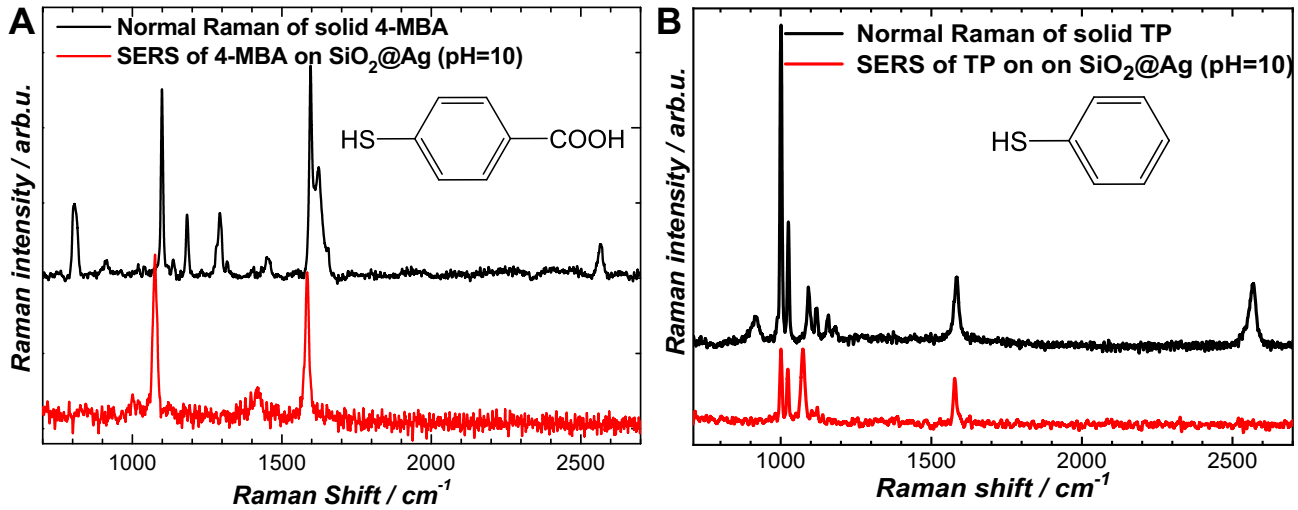

Figure S5. Normal Raman and SERS spectra of (A) 4-MBA and (B) TP. The normal Raman spectra were collected from solid films of the compounds at an excitation power of 5 mW and with a spectral integration time of 30 s. The SERS spectra were collected from individual 4-MBA- or TP-coated SiO_2@Ag SNPs in an aqueous environment at pH of 10 at an excitation power of 2.6 mW with a spectral integration time of 1 s. The molecular structures of the 4-MBA and TP were shown as the insets in panels A and B, respectively. The peaks in the wavenumber range of 2500-2600 cm^{-1} in the normal Raman spectra were assigned to the S-H stretching modes, which completely disappeared in the SERS spectra, indicating that both 4-MBA and TP were chemisorbed on Ag surfaces through covalent Ag-S interactions.

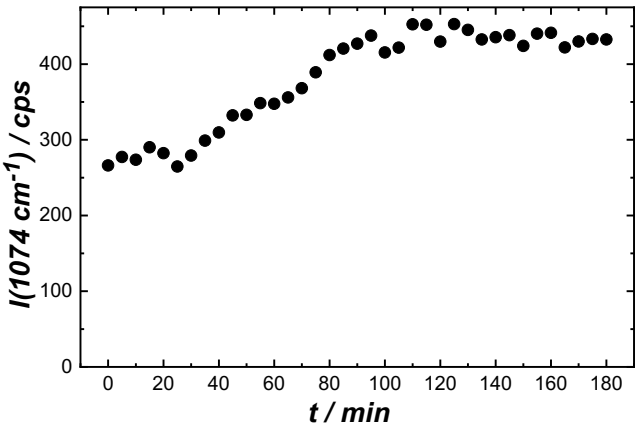

Figure S6. Temporal evolution of the peak intensity at 1074 cm^{-1} in the time-resolved SERS specta shown in Figure 1D. Time-resolved SERS spectra were collected on one 4-MBA-coated SiO_2@Ag SNP upon exposure to 785 nm laser illumination at pH of 10 (in 1.0 mM K_2CO_3). The spectral acquisition time was 5 s, and the laser power was 1.1 mW.

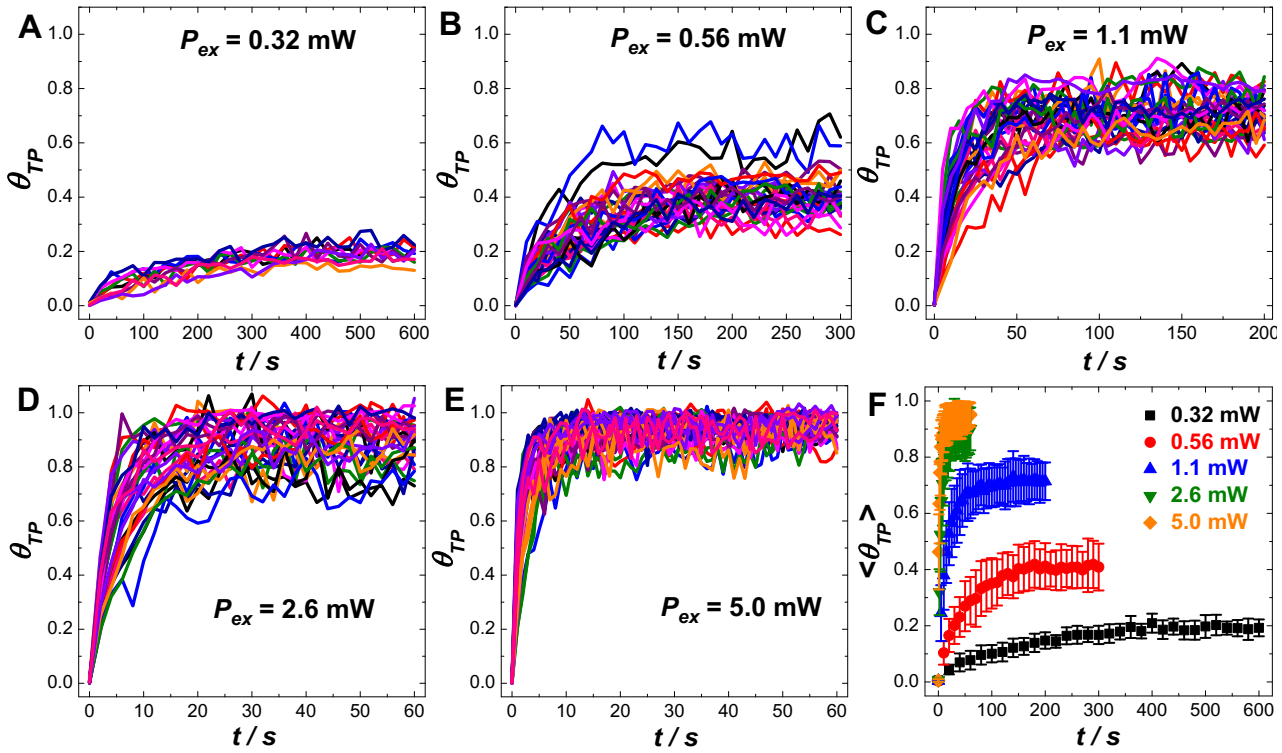

Figure S7. Temproal evolution of θ_{TP} on individual 4-MBA-coated SiO_2@Ag SNPs at various excitation laser powers of (A) 0.32, (B) 0.56, (C) 1.1, (D) 2.6, and (E) 5.0 mW. Each θ_{TP} trajectory represented the kinetic results collected from on one individual 4-MBA-coated SiO_2@Ag SNP under each specific reaction condition. (F) Temporal evolution of ensemble-averaged θ_{TP} ($<\theta_{TP}>$) at various excitation powers. The error bars represent the standard deviations among different particles at each excitation power. In all these experiments, the pH of surrounding solution was kept at 10. The spectral acquisition time was 20 s for 0.32 mW, 10 s for 0.56 mW, 5 s for 1.1 mW, 2 s for 2.6 mW, and 1 s for 5.0 mW, respectively.

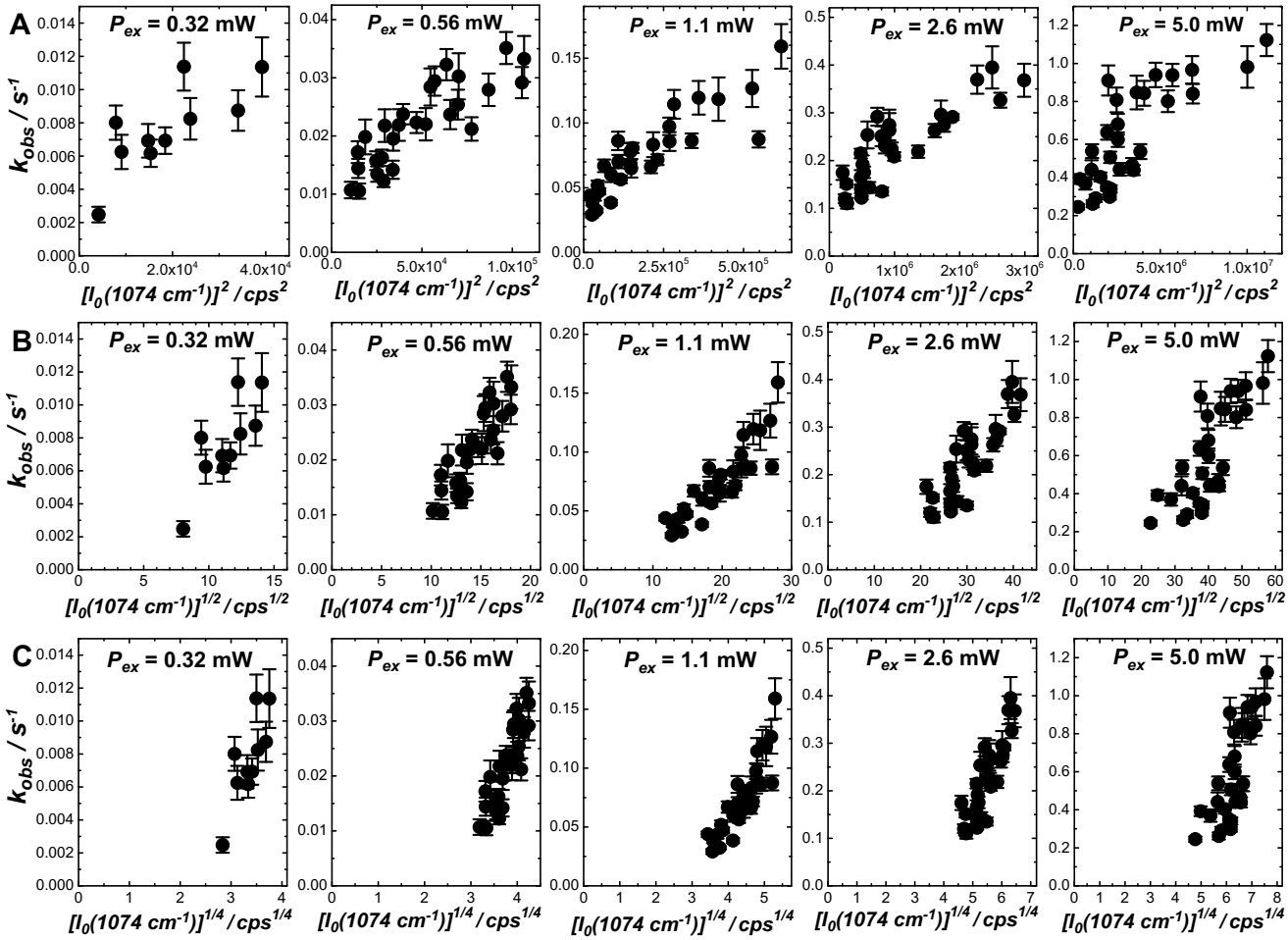

Figure S8. (A) Plots of k_{obs} *vs.* the square of the initial peak intensities of the ν(CS) mode, $[I_0(1074\ cm^{-1})]^2$. (B) Plots of k_{obs} *vs.* the square root of the initial peak intensities of the ν(CS) mode, $[I_0(1074\ cm^{-1})]^{1/2}$. (C) Plots of k_{obs} *vs.* the fourth root of the initial peak intensities of the ν(CS) mode, $[I_0(1074\ cm^{-1})]^{1/4}$. The kinetics measurements were conducted at five different P_{ex} values (0.32, 0.56, 1.1, 2.6, and 5.0 mW), while the excitation wavelgnth, λ_{ex}, was fixed at 785 nm. In all experiments, the pH was maintained at 10. The spectral acquisition time was 20 s for 0.32 mW, 10 s for 0.56 mW, 5 s for 1.1 mW, 2 s for 2.6 mW, and 1 s for 5.0 mW, respectively. At each P_{ex}, the time-resolved SERS results were collected on different individual SiO_2@Ag SNPs one-particle-at-a-time.

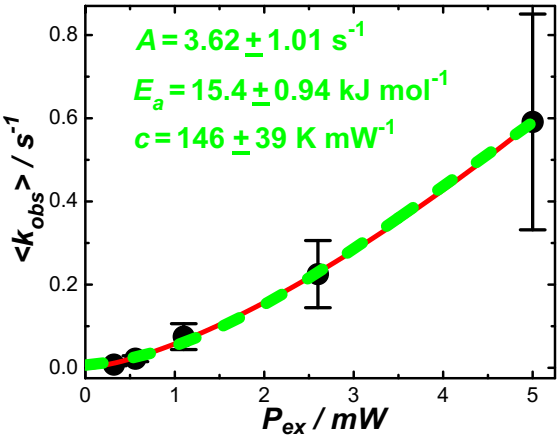

Figure S9. Power-dependence of ensemble-averaged $k_{obs.}$ The green dash curve showed the results when fitting the experimental data with the Arrhenius-type temperature dependence (Eqn. 9) for a photothermal reaction. For comparison, the curve fitting result using the power function (Eqn. 8) for hot carrier-driven photochemistry was shown as the solid red curve.

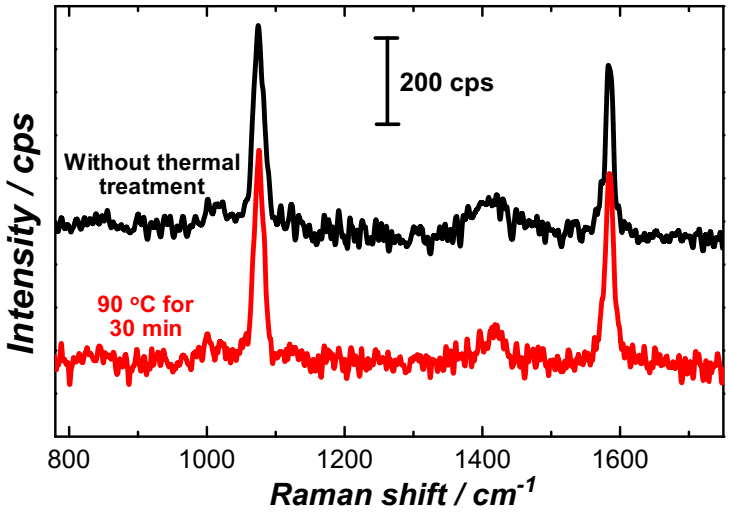

Figure S10. Representative SERS spectra of 4-MBA collected on individual SiO_2@Ag SNPs at pH of 10 (black) without and (red) with thermal heating treatment at 90°C for 30 min. The SERS spectra were collected at room temperature with an P_{ex} of 1.1 mW and a spectral integration time of 5 s.

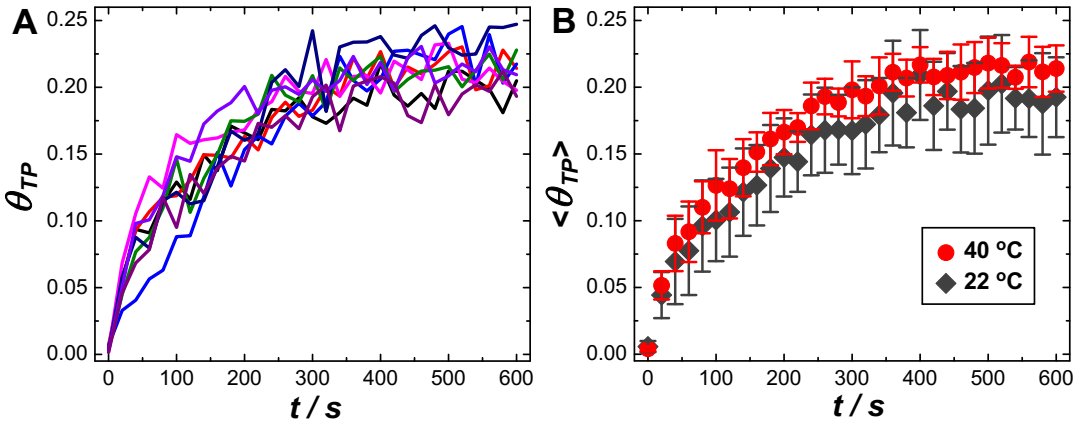

Figure S11. (A) Temporal evolution of θ_{TP} on individual 4-MBA-coated SiO_2@Ag SNPs in water (λ_{ex} = 785 nm; P_{ex} = 0.32 mW) at a reaction temperature of 40 °C. (B) Ensemble averaged θ_{TP} trajectories at room temperature (22 °C) and at a bulk reaction temperature of 40 °C. The SERS spectra were collected at P_{ex} of 0.32 mW and a spectral integration time of 20 s.

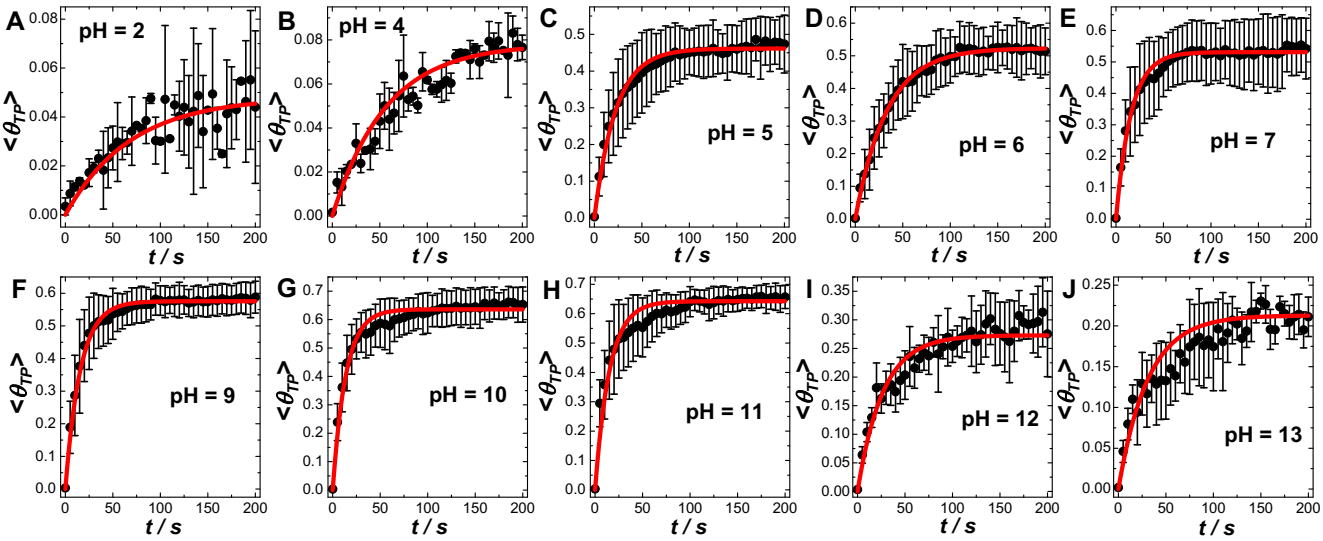

Figure S12. Temperoal evolution of ensemble averaged θ_{TP} ($\langle\theta_{TP}\rangle$) during photocatalytic reactions (λ_{ex} = 785 nm; P_{ex} = 1.1 mW) at different pH values of (A) 2, (B) 4, (C) 5, (D) 6, (E) 7, (F) 9, (G) 10, (H) 11, (I) 12, and (J) 13. The pHs of the reaction medium were adjusted by mixing appropriate amounts of HCl and NaOH in the absence of K_2CO_3. At each pH, the SERS-based kinetic measurements were conducted on 10 different 4-MBA-coated SiO_2@Ag SNPs. The error bars represented the standard deviations among the θ_{TP} trajectories collected form 10 different SiO_2@Ag SNPs at each pH. The $\langle\theta_{TP}\rangle$ trajcetories were fitted with a first-order rate law and the curve fitting results were shown as a red curve in each panel.

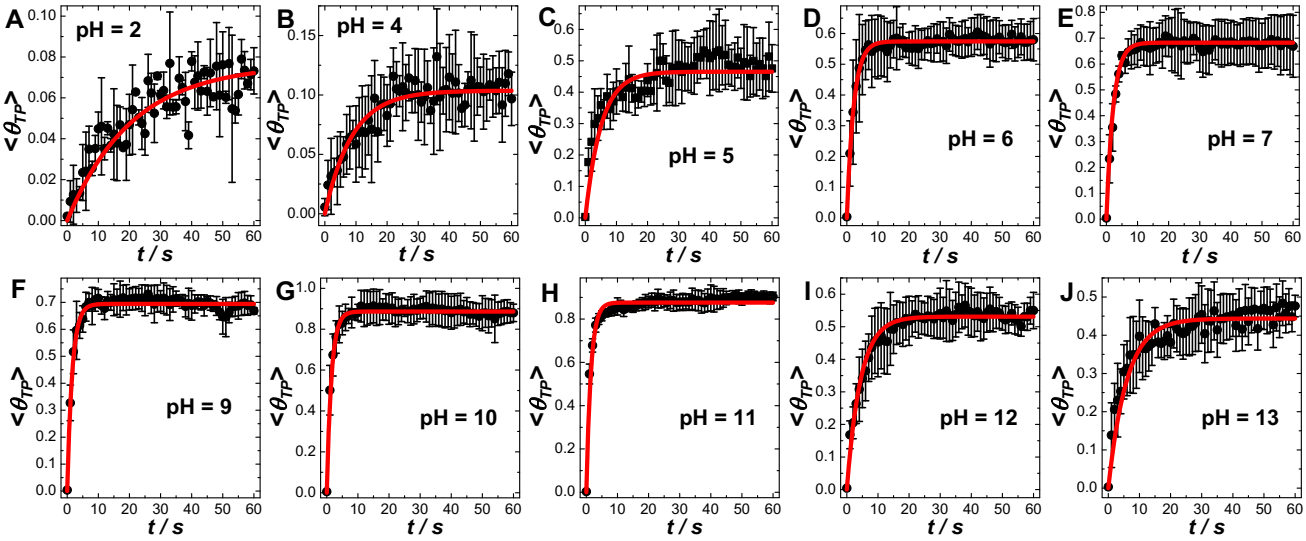

Figure S13. Temperoal evolution of ensemble averaged θ_{TP} ($\langle\theta_{TP}\rangle$) during photocatalytic reactions (λ_{ex} = 785 nm; P_{ex} = 5.0 mW) at different pH values of (A) 2, (B) 4, (C) 5, (D) 6, (E) 7, (F) 9, (G) 10, (H) 11, (I) 12, and (J) 13. The pHs of the reaction medium were adjusted by mixing appropriate amounts of HCl and NaOH in the absence of K_2CO_3. At each pH, the SERS-based kinetic measurements were conducted on 10 different 4-MBA-coated SiO_2@Ag SNPs. The error bars represented the standard deviations among the θ_{TP} trajectories collected form 10 different SiO_2@Ag SNPs at each pH. The $\langle\theta_{TP}\rangle$ trajcetories were fitted with a first-order rate law and the curve fitting results were shown as a red curve in each panel.

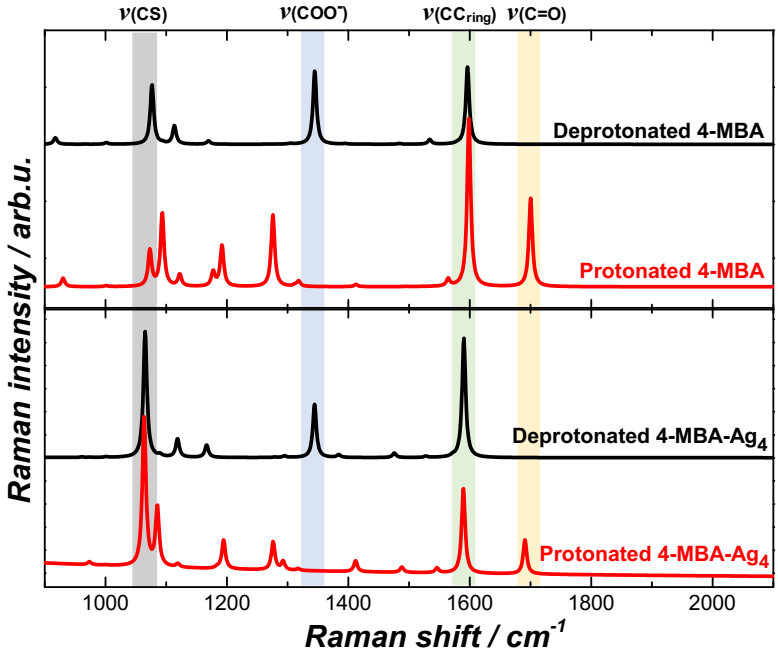

Figure S14. DFT-calculated Raman spectra of deprotonated 4-MBA, protonated 4-MBA, deprotonated 4-MBA-Ag_4, and protonated 4-MBA-Ag_4. The Raman modes of ν(CS), $\nu(COO^-)$, $\nu(CC_{ring})$, and ν(C=O) were highlighted.

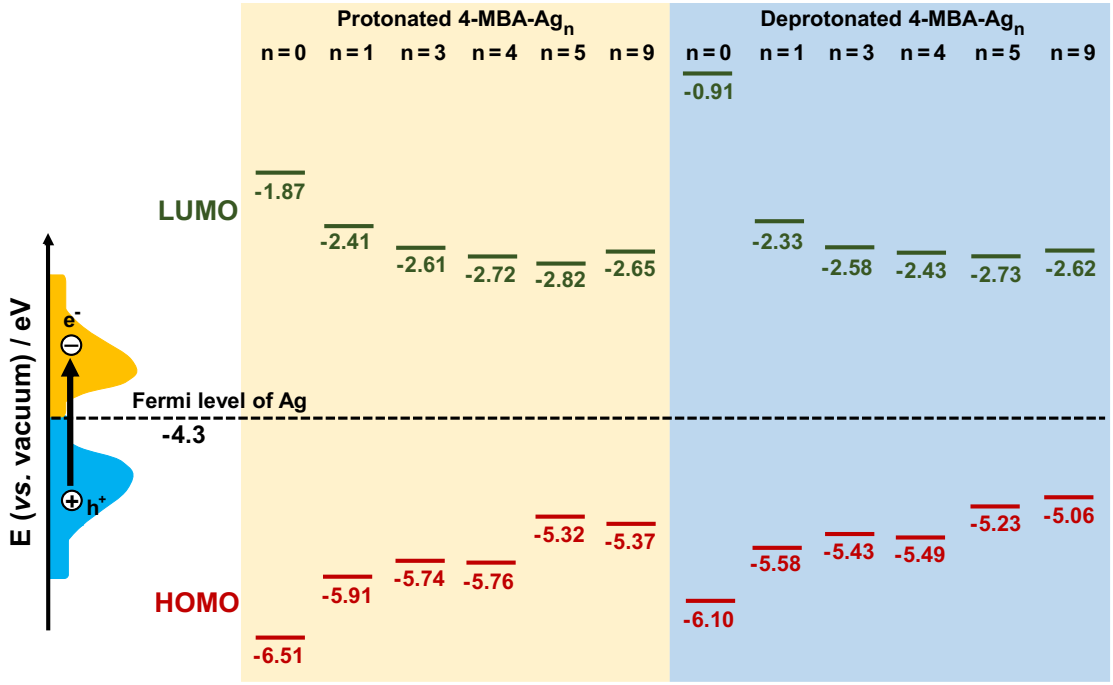

Figure S15. DFT-calcualted energy levels of the LUMO and HOMO of 4-MBA and 4-MBA chemisorbed to Ag_n atomic clusters (n refers to the number of Ag atoms in the clusters) in the protonated and deprotonated forms. The energy diagram was plotted using an energy scale of electron volts (eV) and the vacuum level as the reference.

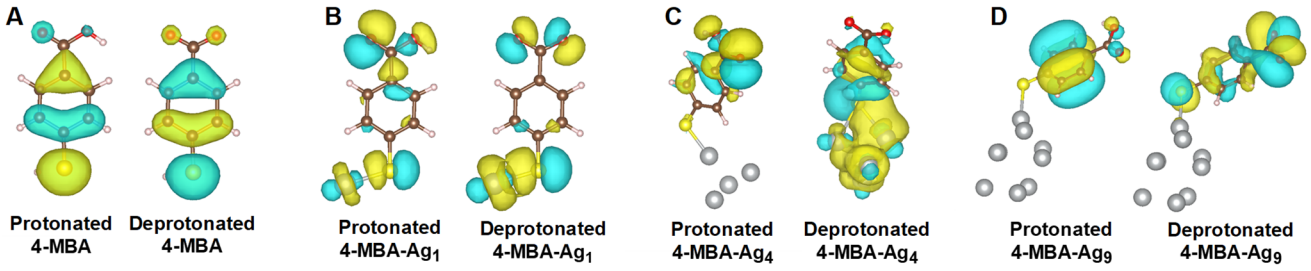

Figure S16. Optimized geometries and electron density maps of the HOMO orbitals of (A) 4-MBA and 4-MBA chemisorbed to (B) an Ag atom, (C) an Ag_4 cluster, and (D) an Ag_9 cluster in the protonated and deprotonated forms.

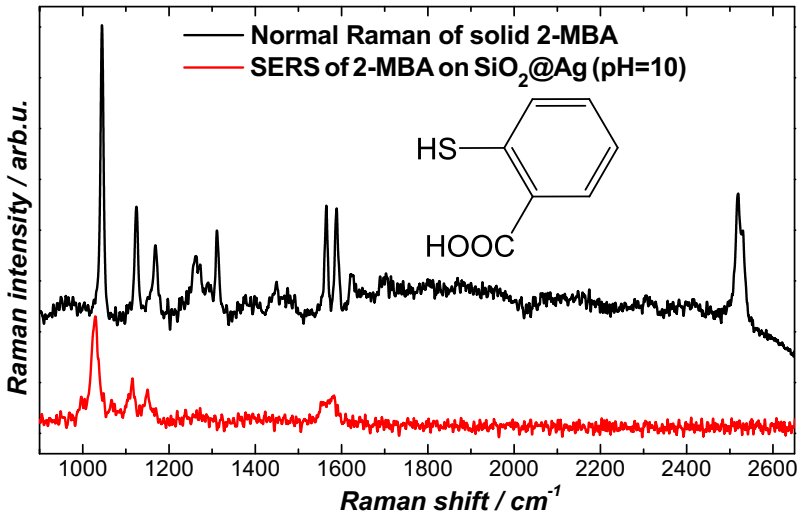

Figure S17. Normal Raman and SERS spectra of 2-MBA. The normal Raman spectrum was collected from a solid 2-MBA film at an excitation power of 5.0 mW and with a spectral integration time of 30 s. The SERS spectrum was collected from an individual 2-MBA-coated SiO_2@Ag SNP in an aqueous environment at pH of 10 at an excitation power of 2.6 mW with a spectral integration time of 1 s. The molecular structure of 2-MBA is shown as the inset. The peak centered around 2530 cm^{-1} in the normal Raman spectrum was assigned to the S-H stretching mode, which completely disappeared in the SERS spectrum, indicating that 2-MBA was chemisorbed on Ag surfaces through covalent Ag-S interactions.

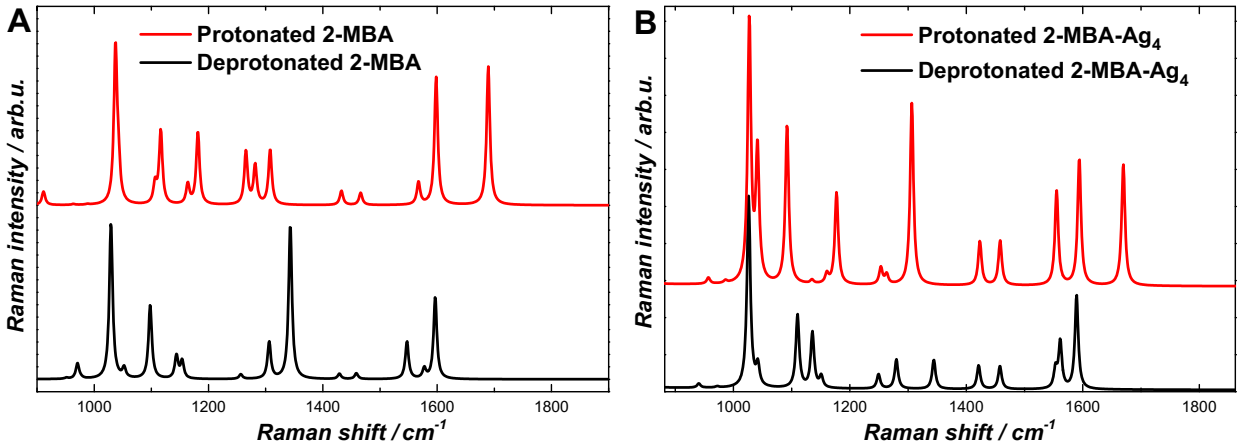

Figure S18. (A) Calculated Raman spectra of deprotonated and protonated 2-MBA. (B) Calculated Raman spectra of deprotonated and protonated 2-MBA-Ag_4.

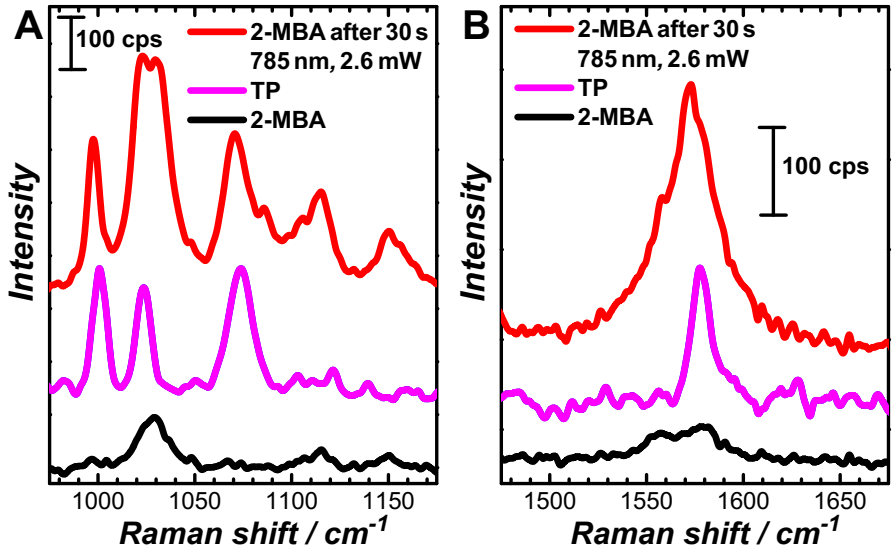

Figure S19. SERS spectra of (black) 2-MBA and (magenta) TP adsorbed on the surfaces of SiO_2@Ag SNPs in the wavenumber ranges of (A) 975-1175 cm^{-1} and (B) 1475-1675 cm^{-1}. The red spectrum was collected from a 2-MBA-coated SiO_2@Ag SNP in 1.0 mM K_2CO_3 after continuous laser illumination (785 nm, 2.6 mW) for 30 s.

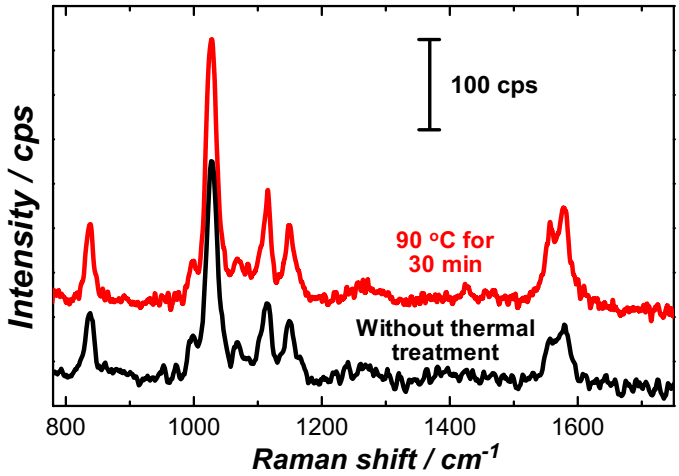

Figure S20. Representative SERS spectra of 2-MBA collected on individual SiO_2@Ag SNPs at pH of 10 (black) without and (red) after thermal heating treatment at 90°C for 30 min. The SERS spectra were collected at room temperature with an P_{ex} of 2.6 mW and a spectral integration time of 1 s.

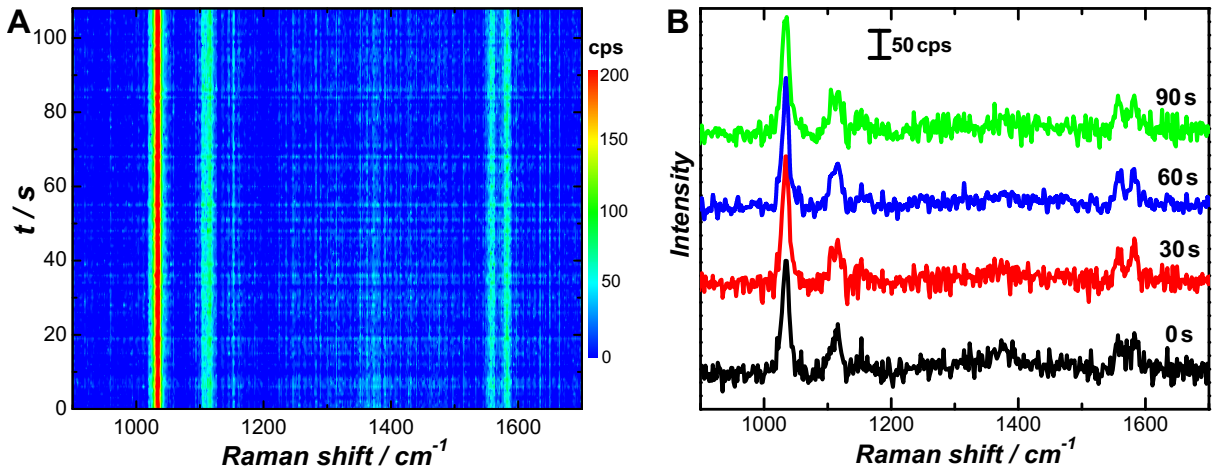

Figure S21. (A) Time-resolved SERS spectra collected on one 2-MBA-coated SiO_2@Ag SNP upon exposure to 785 nm laser illumination at pH of 2. The spectral acquisition time was 1 s, and the laser power was 2.6 mW. (B) Snapshot SERS spectra at reaction times of 0, 30, 60, and 90 s.

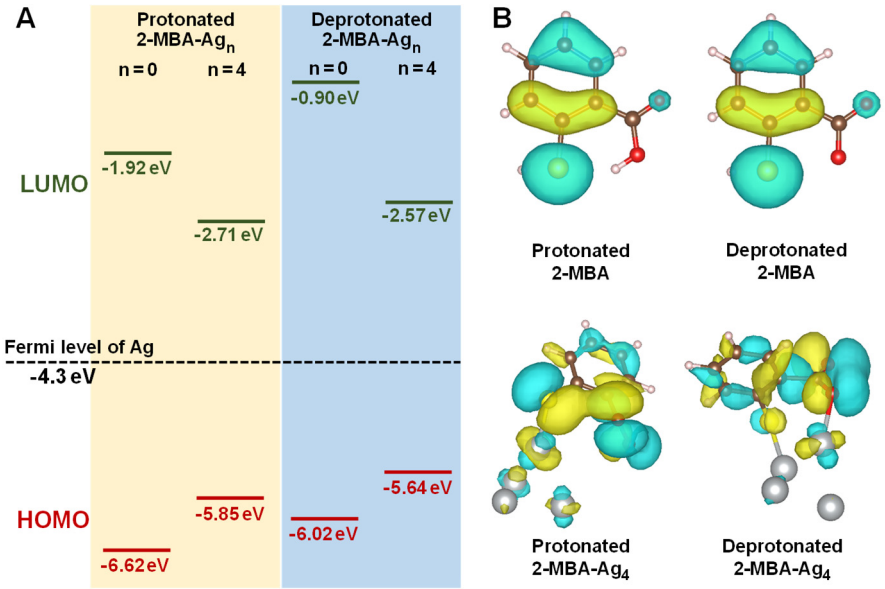

Figure S22. (A) DFT-calcualted energy levels of the LUMO and HOMO of 2-MBA and 2-MBA-Ag_4 in the protonated and deprotonated forms. The energy diagram was plotted using an energy scale of electron volts (eV) and the vacuum level as the reference. (B) Optimized geometries and electron density maps of the HOMO orbitals of 2-MBA and 2-MBA-Ag_4 in the protonated and deprotonated forms.

S3. References for Supporting Information

1. Xia, X. H.; Zeng, J.; Oetjen, L. K.; Li, Q. G.; Xia, Y. N. Quantitative Analysis of the Role Played by Poly(vinylpyrrolidone) in Seed-Mediated Growth of Ag Nanocrystals. *J. Am. Chem. Soc.* **2012,** *134* (3), 1793-1801.

2. Zheng, T. T.; Zhang, Q. F.; Feng, S.; Zhu, J. J.; Wang, Q.; Wang, H. Robust Nonenzymatic Hybrid Nanoelectrocatalysts for Signal Amplification toward Ultrasensitive Electrochemical Cytosensing. *J. Am. Chem. Soc.* **2014,** *136* (6), 2288-2291.

3. Zhang, Q. F.; Wang, H. Mechanistic Insights on Plasmon-Driven Photocatalytic Oxidative Coupling of Thiophenol Derivatives: Evidence for Steady-State Photoactivated Oxygen. *J. Phys. Chem. C* **2018,** *122* (10), 5686-5697.

4. Malynych, S.; Luzinov, I.; Chumanov, G. Poly(vinylpyridine) as a Universal Surface Modifier for Immobilization of Nanoparticles. *J. Phys. Chem. B* **2002,** *106* (6), 1280-1285.

5. Wang, H.; Halas, N. J. Mesoscopic Au "Meatball" Particles. *Adv. Mater.* **2008,** *20* (4), 820-825.

6. Zhang, Q. F.; Large, N.; Nordlander, P.; Wang, H. Porous Au Nanoparticles with Tunable Plasmon Resonances and Intense Field Enhancements for Single-Particle SERS. *J. Phys. Chem. Lett.* **2014,** *5* (2), 370-374.